

2003. Ras GTPases: integrins' friends or foes? *Nat. Rev. Mol. Cell Biol.* 4:767-776.
23. Knox, A. L., and N. H. Brown. 2002. Rap1 GTPase regulation of adherens junction positioning and cell adhesion. *Science* 295:1285-1288.
24. Kouklis, P., M. Konstantoulaki, S. Vogel, M. Broman, and A. B. Malik. 2004. Cdc42 regulates the restoration of endothelial barrier function. *Circ. Res.* 94:159-166.
25. Langeler, E. G., and V. W. van Hinsbergh. 1991. Norepinephrine and iloprost improve barrier function of human endothelial cell monolayers: role of cAMP. *Am. J. Physiol.* 260:C1052-C1059.
26. Lee, M. J., S. Thangada, K. P. Claffey, N. Ancellin, C. H. Liu, M. Kluk, M. Volpi, R. I. Sha'afi, and T. Hla. 1999. Vascular endothelial cell adherens junction assembly and morphogenesis induced by sphingosine-1-phosphate. *Cell* 99:301-312.
27. Lum, H., H. A. Jaffe, I. T. Schulz, A. Masood, A. RayChaudhury, and R. D. Green. 1999. Expression of PKA inhibitor (PKI) gene abolishes cAMP-mediated protection to endothelial barrier dysfunction. *Am. J. Physiol.* 277: C580-C588.
28. Maillet, M., S. J. Robert, M. Cacquevel, M. Gastineau, D. Vivien, J. Bertoglio, J. L. Zugaza, R. Fischmeister, and F. Lezoualc'h. 2003. Crosstalk between Rap1 and Rac regulates secretion of sAPPalpha. *Nat. Cell Biol.* 5:633-639.
29. Milles, A. A., and E. M. Milles. 1952. Vascular reactions to histamine, histamine-liberator and leukotaxine in the skin of guinea-pigs. *J. Physiol.* 118: 228-257.
30. Mochizuki, N., Y. Ohba, E. Kiyokawa, T. Kurata, T. Murakami, T. Ozaki, A. Kitabatake, K. Nagashima, and M. Matsuda. 1999. Activation of the ERK/MAPK pathway by an isoform of rap1GAP associated with G alpha(i). *Nature* 400:891-894.
31. Mori, Y., T. Nishikimi, N. Kobayashi, H. Ono, K. Kangawa, and H. Matsuo. 2002. Long-term adrenomedullin infusion improves survival in malignant hypertensive rats. *Hypertension* 40:107-113.
32. Moy, A. B., J. E. Bodmer, K. Blackwell, S. Shasby, and D. M. Shasby. 1998. cAMP protects endothelial barrier function independent of inhibiting MLC20-dependent tension development. *Am. J. Physiol.* 274:L1024-L1029.
33. Navarro, P., L. Ruco, and E. Dejana. 1998. Differential localization of VE- and N-cadherins in human endothelial cells: VE-cadherin competes with N-cadherin for junctional localization. *J. Cell Biol.* 140:1475-1484.
34. Ohba, Y., K. Ikuta, A. Ogura, J. Matsuda, N. Mochizuki, K. Nagashima, K. Kurokawa, B. J. Mayer, K. Maki, J. Miyazaki, and M. Matsuda. 2001. Requirement for C3G-dependent Rap1 activation for cell adhesion and embryogenesis. *EMBO J.* 20:3333-3341.
35. Parandoosh, Z., C. A. Bogowitz, and M. P. Nova. 1998. A fluorometric assay for the measurement of endothelial cell density in vitro. *In Vitro Cell. Dev. Biol. Anim.* 34:772-776.
36. Price, L. S., A. Hajdo-Milasinovic, J. Zhao, F. J. Zwartkruis, J. G. Collard, and J. L. Bos. 2004. Rap1 regulates E-cadherin-mediated cell-cell adhesion. *J. Biol. Chem.* 279:35127-35132.
37. Quilliam, L. A., H. Mueller, B. P. Bohl, V. Prossnitz, L. A. Sklar, C. J. Der, and G. M. Bokoch. 1991. Rap1A is a substrate for cyclic AMP-dependent protein kinase in human neutrophils. *J. Immunol.* 147:1628-1635.
38. Shaywitz, A. J., and M. E. Greenberg. 1999. CREB: a stimulus-induced transcription factor activated by a diverse array of extracellular signals. *Annu. Rev. Biochem.* 68:821-861.
39. Stelzner, T. J., J. V. Weil, and R. F. O'Brien. 1989. Role of cyclic adenosine monophosphate in the induction of endothelial barrier properties. *J. Cell. Physiol.* 139:157-166.
40. Ukropec, J. A., M. K. Hollinger, S. M. Salva, and M. J. Woolkalis. 2000. SHP2 association with VE-cadherin complexes in human endothelial cells is regulated by thrombin. *J. Biol. Chem.* 275:5983-5986.
41. Yajnik, V., C. Paulding, R. Sordella, A. I. McClatchey, M. Saito, D. C. Wahrer, P. Reynolds, D. W. Bell, R. Lake, S. van den Heuvel, J. Settleman, and D. A. Haber. 2003. DOCK4, a GTPase activator, is disrupted during tumorigenesis. *Cell* 112:673-684.
42. Yano, H., Y. Mazaki, K. Kurokawa, S. K. Hanks, M. Matsuda, and H. Sabe. 2004. Roles played by a subset of integrin signaling molecules in cadherin-based cell-cell adhesion. *J. Cell Biol.* 166:283-295.
43. Yuan, S. Y. 2002. Protein kinase signaling in the modulation of microvascular permeability. *Vascul. Pharmacol.* 39:213-223.

Identification and Characterization of Zipper-interacting Protein Kinase as the Unique Vascular Smooth Muscle Myosin Phosphatase-associated Kinase*

Received for publication, April 2, 2004, and in revised form, July 13, 2004
Published, JBC Papers in Press, July 30, 2004, DOI 10.1074/jbc.M403676200

Akira Endo[‡], Howard K. Surks[‡], Seibu Mochizuki[§], Naoki Mochizuki[¶],
and Michael E. Mendelsohn[‡]

From the [‡]Molecular Cardiology Research Institute, New England Medical Center and Department of Medicine, Tufts University School of Medicine, Boston, Massachusetts, the [§]Division of Cardiology, Department of Internal Medicine, Jikei University School of Medicine, Minato-ku, Tokyo 105-8461, Japan, and the [¶]Department of Structural Analysis, National Cardiovascular Center Research Institute, Suita, Osaka 565-8565, Japan

Excitation-contraction coupling in smooth muscle involves activation of myosin light chain (MLC) phosphorylation, which increases activity of the myosin actin-activated ATPase, resulting in contraction. Phosphorylation of MLC phosphatase (SMPP-1M) by Rho-associated kinase or endogenous SMPP-1M-associated kinase inhibits SMPP-1M, enhancing MLC phosphorylation and contraction. However, the precise identity of SMPP-1M-associated kinase remains unclear. Biochemical evidence strongly supports the idea that SMPP-1M-associated kinase is related to the human serine/threonine leucine zipper-interacting protein kinase (hZIPK), which is important in cell apoptosis, and the SMPP-1M-associated kinase has therefore been called ZIP-like kinase (MacDonald, J. A., Borman, M. A., Murani, A., Somlyo, A. V., Hartshorne, D. J., and Haystead, T. A. J. (2001) *Proc. Natl. Acad. Sci. U. S. A.* 98, 2419–2424). Whether the vascular smooth muscle SMPP-1M-associated kinase is a truncated version of hZIPK, native hZIPK, or a unique homologue of hZIPK is unclear. Here we show that only native hZIPK mRNA and protein are detectable in human vascular smooth muscle cells (VSMCs). High stringency screening of a human aortic cDNA library for the SMPP-1M-associated kinase identified 18 positive clones, all of which proved to be clones of hZIPK. PCR-based studies of VSMC RNA revealed native hZIPK transcripts but no evidence for splice variants of hZIPK or a ZIP-like kinase. Northern blotting studies of multiple vascular and non-vascular tissue RNAs, including human bladder RNA, showed only 2.3 kb of mRNA predicted for full-length hZIPK. Immunoblotting showed native full-length 52-kDa hZIPK expression in VSMCs. Full-length and N-terminal hZIPK bound the C-terminal domain (amino acids 681–847) of the myosin binding subunit (MBS) of SMPP-1M. hZIPK immunoprecipitated with the MBS of SMPP-1M and dominant negative RhoA inhibited the hZIPK-MBS interaction. These data identify hZIPK as the unique SMPP-1-associated kinase expressed in human vesicular smooth muscle and support a role for Rho in promoting the hZIPK-MBS interaction.

Blood vessel tone regulates blood pressure and flow and is itself dynamically regulated by the contractile state of vascular smooth muscle cells (VSMCs) in the blood vessel wall. Contraction and relaxation of VSMCs is determined by the phosphorylation state of myosin light chains (MLCs), a process that is tightly regulated by the opposing activities of myosin light chain kinase and myosin phosphatase (SMPP-1M) (1, 2). Myosin phosphatase is the critical enzyme that dephosphorylates MLC, leading to cell relaxation (3).

In recent years, accumulating evidence supports the view that myosin phosphatase activity is highly regulated. Nitrovasodilators, via cGMP and cGMP-dependent protein kinase I α , lead to activation of PP1M and cell relaxation (4–8). Vasoconstrictors, conversely, increase MLC phosphorylation by at least two pathways, namely activation of MLCK (9, 10) and inhibition of SMPP-1M. Vasoconstrictors can inhibit SMPP-1M by activation of the potent PP1M inhibitor CPI-17 (11, 12) or via RhoA-mediated SMPP-1M phosphorylation (13). RhoA, when activated by vasoconstrictors, binds and activates its effector Rho-kinase, which leads to SMPP-1M phosphorylation (13). Although the mechanism by which RhoA and Rho-kinase are targeted to SMPP-1M on contractile fibers is unclear, both RhoA and SMPP-1M have been shown recently to interact with the actin-binding protein M-RIP (14).

Biochemical isolation of SMPP-1M has led to the recovery of SMPP-1M-associated kinase activity (15–19). The SMPP-1M-associated kinase phosphorylates the myosin binding subunit (MBS) of SMPP-1M and inhibits SMPP-1M activity. As recent data support the physiologic importance of SMPP-1M regulation, attention has focused on identification of the SMPP-1M-associated kinase(s).

Recently, MacDonald *et al.* identified a SMPP-1M-associated kinase and named it ZIP-like kinase. ZIP-like kinase was isolated from bladder smooth muscle as a 32-Da phosphoprotein that co-purified with SMPP-1M, phosphorylated SMPP-1M at inhibitory residues, and was activated by the smooth muscle contractile agonist carbachol (16). Furthermore, introduction of ZIP-like kinase into rabbit ileal smooth muscle led to calcium-independent contractions (20).

Despite data supporting a physiological role for a ZIP-like kinase in smooth muscle, the precise identity of this kinase and

* This work was supported in part by National Institutes of Health Grant ML55309 (to M. E. M.) and a fellowship grant from the Uehara Memorial Foundation (to A. E.). The costs of publication of this article were defrayed in part by the payment of page charges. This article must therefore be hereby marked "advertisement" in accordance with 18 U.S.C. Section 1734 solely to indicate this fact.

‡ To whom correspondence should be addressed. E-mail: mmendelsohn@tufts-nemc.org.

¹ The abbreviations used are: VSMC, vascular smooth muscle cell; aa, amino acid(s); GST, glutathione S-transferase; HEK293, human embryonic kidney 293 (cell); MBS, myosin-binding subunit; MLC, myosin light chain; SMPP-1M, MLC phosphatase; MOPS, 4-morpholinepropanesulfonic acid; ZIPK, zipper-interacting protein kinase; hZIPK, human ZIPK.

its presence and function in VSMCs remains unclear. Sequencing of ZIP-like kinase-derived peptides revealed high homology to the 52-kDa zipper-interacting protein kinase (hZIPK), raising the possibility that ZIP-like kinase could be a splice variant of hZIPK, a separate kinase with high homology to hZIPK, or a degradation product of hZIPK (16). hZIPK was identified originally as a protein involved in programmed cell death that interacts with the transcription factor ATF4 and mediates apoptosis when overexpressed (21). hZIPK has also been shown to have a potential role in regulating VSMC contraction. hZIPK was found to phosphorylate MLC at both Ser¹⁹ and Thr¹⁸ in a calcium-independent manner, leading to cell contraction (22).

The following study was initiated to determine the precise identity of the PP1M-associated kinase(s) in VSMCs. Through a combination of mRNA and protein analysis, we have found evidence to strongly support the proposition that "ZIP-like kinase" in VSMCs is actually derived from hZIPK, which is present in VSMCs and interacts with SMPP-1M in a RhoA-regulated manner.

MATERIALS AND METHODS

Antibodies—Sources of antibodies were as follows. The rabbit polyclonal anti-ZIP kinase (amino acids 279–298) was from Calbiochem, the anti-FLAG-M2 antibody was from Sigma, the anti-myosin phosphatase polyclonal antibody came from Covance (Berkeley, CA), and normal mouse IgG and normal rabbit IgG were from Santa Cruz Biotechnology Inc., Santa Cruz, CA.

Cell Culture and Transfection—Human embryonic kidney 293 (HEK293) cells were purchased from the American Type Culture Collection (Manassas, VA). Immortalized aorta smooth muscle cells, coronary smooth muscle cells, pulmonary artery smooth muscle cells, and radial artery smooth muscle cells were developed in our laboratory from human tissues by the explant method. These cells were cultured in Dulbecco's modified Eagle's medium supplemented with 10% fetal calf serum. HEK293 cells were transfected by the calcium phosphate method.

Plasmids—To generate plasmids expressing hZIPK, cDNA-fragments were amplified by a polymerase chain reaction from pACT2 (Clontech) containing hZIPK fragments and cloned into pT7Blue-3 (Novagen, Madison, WI). pT7Blue3-hZIPK was digested with EcoRI and BamHI, and the fragments were cloned into the pFLAG-CMV4 vector (Sigma). GST fusion proteins of full-length and C-terminal hZIPK were generated as follows. DNA fragments corresponding to full-length and C-terminal hZIPK were amplified by PCR using the primer pairs of 5'-GGGAATTCATGTCCACGTTCCAGCCAGCAG-3' (5') and 5'-GGCTCGACCTAGCGCAGCCCGCACTCCACG-3' (3') for the former and 5'-GGGAATTCAGCGCCGCAAGCCGAGCCGGC-3' (5') and 5'-GGCTCGACCTAGCGCAGCCCGCACTCCACG-3' (3') for the latter. The PCR products were cloned into pT7Blue-3 and digested with EcoRI and SalI. These fragments were cloned into pGEX4T-3 and pGEX4T-1 vectors (Amersham Biosciences). To generate the plasmid expressing the GST-N-terminal region of hZIPK, NotI-digested pGEX4T-3 hZIPK was treated with a Klenow fragment (New England Biolabs, Beverly, MA) to blunt the ends, followed by self-ligation. pEF-BOS-mouse ZIPK was a gift from S. Akira, Department of Biochemistry, Hyogo College of Medicine. pCXN₂-IRES-EGFP (23) expression vectors were derived from pCAGGS and contain the internal ribosomal entry site (IRES) and the coding region of the enhanced green fluorescent protein (EGFP) at the 3'-end of the multiple cloning site. The cDNA fragments encoding the small GTPase RhoA, RhoN19 (dominant negative form), and RhoQ63L (constitutively active form) were amplified by polymerase chain reaction and subcloned into pCXN₂-IRES-EGFP.

Human Aorta cDNA Library Screening—A human aorta cDNA library containing 3.5×10^6 independent clones (Clontech) was screened by the colony hybridization technique (24). ³²P-labeled EcoRI-NotI fragments of hZIPK cDNA were made from the cDNA clone AI660136 (Genome System) encoding the N terminus of hZIPK and used as a probe. The library was transferred to Hybond N synthetic nylon membranes (Amersham Biosciences) and then pre-hybridized and hybridized in 5× Denhardt's solution, 5× SSC, 0.1 M sodium phosphate, 0.5% SDS, and 100 µg/ml denatured salmon sperm DNA under high (hybridization temperature 65 °C) and low (hybridization temperature 58 °C) stringency conditions.

Polymerase Chain Reaction—PCR was performed in a final volume of 50 µl of reaction mix containing 0.2 mM each dNTP, 1.5 mM MgCl₂, PCR

buffer without magnesium, 0.25 µM each primer for the investigation of ZIPK splice variants, 500 µM each primer for degenerate PCR, and 2 units of Taq DNA polymerase (Invitrogen). Reaction mixtures were heated for 5 min at 95 °C, followed by 30 cycles of amplification. Each cycle consisted of denaturation at 95 °C for 30 s, annealing between 38 and 57 °C, and extension at 70 °C between 1 and 3 min. After the last cycle, samples were incubated for an additional 10 min at 70 °C. The following primers were designed for the investigation of hZIPK splice variants: primer 1, 5'-AGCGCGCTCGCGCCGCGCAGGCCG-3' (3') and 5'-CTTCAGGTCAAAGTGTGCGATGCG-3' (5'); primer 2, 5'-AGCGCGCTCGCGCCGCGCAGGCCG-3' (3') and 5'-GGATATAGGTGATGACACCGA-3' (5'); primer 3, 5'-AGCGCGCTCGCGCCGCGCAGGCCG-3' (3') and 5'-GCTCGGCTTGCAGCCGCTG-3' (5'); primer 4, 5'-ATCTCCACGTTCCAGGCAGGAGG-3' (3') and 5'-CTTCAGGTCAAAGTGTGCGATGCG-3' (5'); primer 5, 5'-ATGTCCACGTTCCAGGCAGGAGG-3' (3') and 5'-GGATATAGGTGATGACACCGA-3' (5'); primer 6, 5'-ATGTCCACGTTCCAGGCAGGAGG-3' (3') and 5'-GCTCGGCTTGCAGCCGCTG-3' (5'); primer 7, 5'-AGGAACAGAGCCCTGCC-3' (3') and 5'-CTTCAGGTCAAAGTGTGCGATGCG-3' (5'); primer 8, 5'-AGGAACAGAGCCCTGCC-3' (3') and 5'-GGATATAGGTGATGATGACACCGA-3' (5'); primer 9, 5'-AGGAACAGAGCCCTGCC-3' (3') and 5'-CTTCAGGTCAAAGTGTGCGATGCG-3' (5'); primer 10, 5'-ATGCTGTGGACAAGAAC-3' (3') and 5'-GGATATAGGTGATGACACCGA-3' (5'); and primer 11, 5'-ATGCTGTGGACAAGAAC-3' (3') and 5'-CTTCAGGTCAAAGTGTGCGATGCG-3' (5') (Fig. 3). Exons were predicted using the NCBI LocusLink program.

The following primers were used for degenerate PCR: primer IA, 5'-ATGGGNGARGARYTNGG-3' (5') and 5'-YTGDATNGGNC-3' (3'); primer IB, 5'-ATGGGNGARGARYTNGG-3' (5') and 5'-RAADATNNNYTTRTC-3' (3'); primer IIA, 5'-GAYAARNNNATHHTT-3' (5') and 5'-ARRTTYTGNGCDAT-3' (3'); primer IIB, 5'-MGNCCNATHCA-3' (5') and 5'-ARRTTYTGNGCDAT-3' (3'); primer III, 5'-ATGGGNGARGARYTNGG-3' (5') and 5'-ARRTTYTGNGCDAT-3' (3') (Fig. 2). The primers 5'-ATGGGNGARGARYTNGG-3', 5'-GAYAARNNNATHHTT-3', 5'-MGNCCNATHCA-3', 5'-YTGDATNGGNC-3', 5'-RAADATNNNYTTRTC-3', and 5'-ARRTTYTGNGCDAT-3' corresponded to amino acid sequences MGEEL, DKXIF, RPIQ, QIPR, FIXKD, and LNQA, respectively. The human aorta cDNA library was used as the template for PCR with IA, IIA, and III. PCR products from IA and IIA were used as the template for PCR with IB and IIB, respectively.

RNA Expression Analysis by Northern Blotting—Total RNA from a series of mouse tissues and poly(A)⁺ RNA from cultured cells and human bladder was electrophoresed in an agarose gel containing 2% formaldehyde and 20 mM MOPS and blotted onto Hybond N synthetic nylon membrane (Amersham Biosciences). A multiple tissue Northern blot that has poly(A)⁺ RNA from a series of human tissues was purchased from Clontech. The membranes were pre-hybridized and hybridized in ExpressHyb hybridization solution (Clontech) with [³²P]dCTP-labeled probe. The cDNA probes used in this study are described as follows. A 0.9-kb EcoRI-NotI fragment encoding the 5'-end of the human ZIPK cDNA and a 1.4-kb EcoRI-BamHI fragment encoding full-length human ZIPK were made from pFLAG-CMV4-ZIPK. A 1-kb SalI-NotI fragment encoding the 5'-end of mouse ZIPK and a 1.3-kb SalI-SalI fragment encoding full-length mouse ZIPK were made from pEF-BOS-ZIPK.

Preparation of GST Fusion Proteins for Binding Studies—BL21 cells were transformed with GST-ZIPK plasmids, described above, and GST-MBS plasmids expressing the C-terminal 183 aa of MBS or the C-terminal 183 aa in which the four leucine residues of the leucine zipper domain have been mutated to alanines (L1007A, L1014A, L1021A, and L1028A) were made as described previously (14). The transformed cells were grown in Luria-Bertani media at 30 °C until the absorbance at 600 nm reached 0.6–0.8. Protein expression was induced by the addition of 0.1 mM isopropyl-β-D-thiogalactopyranoside for 3 h, and GST fusion proteins were isolated by using glutathione-Sepharose 4B beads.

Immunoprecipitation, Immunoblotting, and Cell Staining—Cells were washed with ice-cold Tris-buffered saline (25 mM Tris-HCl, pH7.5, and 150 mM NaCl), and lysed in lysis buffer (20 mM Tris-HCl, pH7.5, 137 mM NaCl, 1% Triton X-100, 2 mM EDTA, 10% glycerol, 25 mM β-glycerophosphate, protease inhibitor mixture set III (Calbiochem), and protease inhibitor mixture tablets (Roche Applied Science). Lysates were cleared by centrifugation at 15,000 × g for 10 min. Aliquots of total cell lysate were subjected to immunoblotting with antibodies as indicated in Figs. 1 and 5–7. The remaining cell lysate was subjected to either immunoprecipitation using antibodies as indicated in Figs. 6 and 7 and protein A- and G-Sepharose (Amersham Biosciences) or GST fusion protein interaction studies by incubation with the indicated GST fusion protein. This treatment was followed by SDS-PAGE and transfer

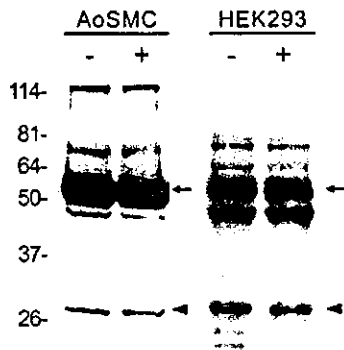


FIG. 1. Expression of the ZIPK protein in HEK293 cells and human vascular smooth muscle cells. HEK293 cell lysates from cells transfected with ZIPK cDNA and native human aortic smooth muscle cell lysates (AoSMC) (10 μ g) were separated by SDS-PAGE with (+) and without (-) protease inhibitors present and immunoblotted with the polyclonal anti-ZIPK antibody. Arrow and arrowhead indicate ZIPK at the 52- and a 32-kDa band recognized by the antibody, respectively. The ZIP-like kinase co-purified with SMPP-1M from bladder smooth muscle was a 32-kDa protein (16).

to polyvinylidene difluoride membranes. The blocked membranes were incubated with the primary antibody at 4 °C overnight and then probed with the secondary antibody linked to peroxidase. Immunoreactive bands were visualized by a chemiluminescence system (Amersham Biosciences) and subjected to densitometric quantitation. For immunofluorescence labeling, cells were washed with phosphate-buffered saline, fixed by 4% paraformaldehyde at room temperature, and then permeabilized with 0.1% Triton X-100. Permeabilized cells were incubated with an anti-FLAG antibody followed by Alexa 488 goat anti-mouse IgG (Molecular Probes, Eugene, OR).

Statistical Analysis—Data are presented as means \pm S.E. Statistical difference was evaluated by Student's *t* test. A *p* value of < 0.01 was regarded as significant.

RESULTS

Immunoblotting Studies—A 32-kDa SMPP-1M-associated kinase was detected previously by immunoblotting of rabbit bladder lysates with the anti-hZIPK antibody (16). We have used this antibody in immunoblotting studies of proteins expressed by native vascular smooth muscle cells and in studies of HEK293 cells expressing the cDNA for hZIPK (Fig. 1). In both VSMC cells and in heterologous expression studies of HEK293 cells the most prominent protein band detected by the anti-ZIPK antibody was 52 kDa (Fig. 1, upper arrows). A 32-kDa band was also detected in both cell types (arrowhead) but was less prominent, especially in human VSMC lysates. The inclusion of protease inhibitors did not alter the amount of 32-kDa protein detected (+ lanes, Fig. 1). In the HEK293 cells expressing hZIPK, another protein of ~48 kDa was also prominent. Detection of this 48-kDa protein was also not affected by the inclusion of a mixture of protease inhibitors.

cDNA Library Screening for ZIPK and ZIP-like Kinase—A human aorta cDNA library containing 3.5×10^6 independent clones was screened for the presence of ZIPK and ZIP-like kinase by the colony hybridization technique. A 981-bp fragment of the 5'-end of hZIPK was used as the probe. This region of hZIPK cDNA was chosen for the probe design based on a previous report of homology between peptide fragments of ZIP-like kinase and the amino-terminal kinase domain of ZIPK (16) (Fig. 2A). The human aorta cDNA library was screened under both high and low stringency conditions. Using high stringency conditions, we obtained 18 positive clones. These positive clones were fully sequenced, and all 18 positive clones were identified as either full-length or fragments of hZIPK. Under low stringency conditions, 41 positive clones were obtained, and 31 were identified as full-length or fragments of hZIPK. We also cloned myosin light chain kinase (eight clones), the kinase

domain of which has 48% amino acid sequence identity and 59% nucleotide sequence identity (25), as well as part of the ZIPK gene on chromosome 19 (two clones). ZIP-like kinase was not identified by either of the library screens.

PCR Studies to Search for ZIP-like Kinase and Detect Potential ZIPK Splice Variants—We designed degenerate PCR primers corresponding to the three peptide sequences derived originally from ZIP-like kinase with minor or uncertain sequence differences from hZIPK (Fig. 2B) (16). All DNA fragments amplified from the human aorta library using these degenerate primers were sequenced (Fig. 2C) but proved to be nonspecific, and no sequences corresponded to those of hZIPK or ZIP-like kinase.

To determine whether ZIP-like kinase is a splice variant of hZIPK, we searched for hZIPK splice variants in the human aorta cDNA library. hZIPK mRNA is derived from eight exons on chromosome 19. We designed PCR primers corresponding to each exon and two putative exons designated potential exons A and B, one 5' to exon 1 (potential exon A) and the other between exon 2 and exon 3 (potential exon B) (Fig. 3A) based on predicted potential splice sites and variants (the NCBI LocusLink program). PCR was performed with 11 primer pairs designed to amplify both the known exons and potential exons A and B. Only the hZIPK exons were amplified. A number of DNA fragments were sequenced and proved to be of 100% identity to hZIPK (Fig. 3B). These results make the existence of a potential splice variant in human aorta of hZIPK unlikely.

Northern Blotting Studies—We investigated the expression of mRNA encoding ZIP-like kinase in various human tissues and cultured cells by performing Northern blot analyses. In all of these human tissues and cultured cells, a 5'-probe, based on hZIPK, was used at moderate stringency to detect hZIPK and any related transcripts. In all tissues and cells examined, a 2.3-kb band consistent with the predicted size of the hZIPK transcript was present, but no evidence of any other transcripts was noted (Fig. 4, A and B). ZIP-like kinase was co-purified with SMPP-1M originally from bladder smooth muscle (16). We therefore obtained human bladder tissue, isolated the mRNA, and performed separate Northern blot experiments (Fig. 4B, right panel). In human bladder, only a 2.3-kb band consistent with the predicted size of the hZIPK transcript was detected, and no evidence of any other transcript was noted. Re-probing of these blots with full-length hZIPK probe led to detection of the same bands and no others, indicating that these 2.3-kb bands are hZIPK mRNA (data not shown). We also investigated hZIPK and ZIP-like kinase expression in various mouse tissues, including brain, aorta, heart, lung, liver, spleen, kidney, uterus, and bladder. Among the mouse tissues, an ~2.3-kb band was detected. No other smaller mRNA species were detected (data not shown). We therefore could find no evidence that suggested the existence of an mRNA for a ZIP-like kinase in human and mouse tissues or in cultured cells.

Interaction of hZIPK with MBS—We investigated whether full-length hZIPK interacts with MBS. FLAG-tagged hZIPK was well expressed in HEK293 cells and distributed uniformly throughout the cytoplasm in these cells (Fig. 5, A and B). FLAG-hZIPK bound the C-terminal half of human MBS (GST-MBS with aa 681–1030). In contrast, neither GST-MBS with aa 847–1030 nor a mutant GST-MBS with aa 847–1030 in which the leucine zipper of MBS is disrupted by alanine substitution (designated GST-MBS 847–1030 LZM in Fig. 5) bound hZIPK. These data confirm an *in vitro* interaction between full-length hZIPK and the coiled coil-containing domain of MBS (aa 681–847 of human MBS) (Fig. 5C). The binding of native ZIPK from human vascular smooth muscle cells to these GST-MBS fusion proteins was similarly observed (Fig. 5E). In reciprocal studies,

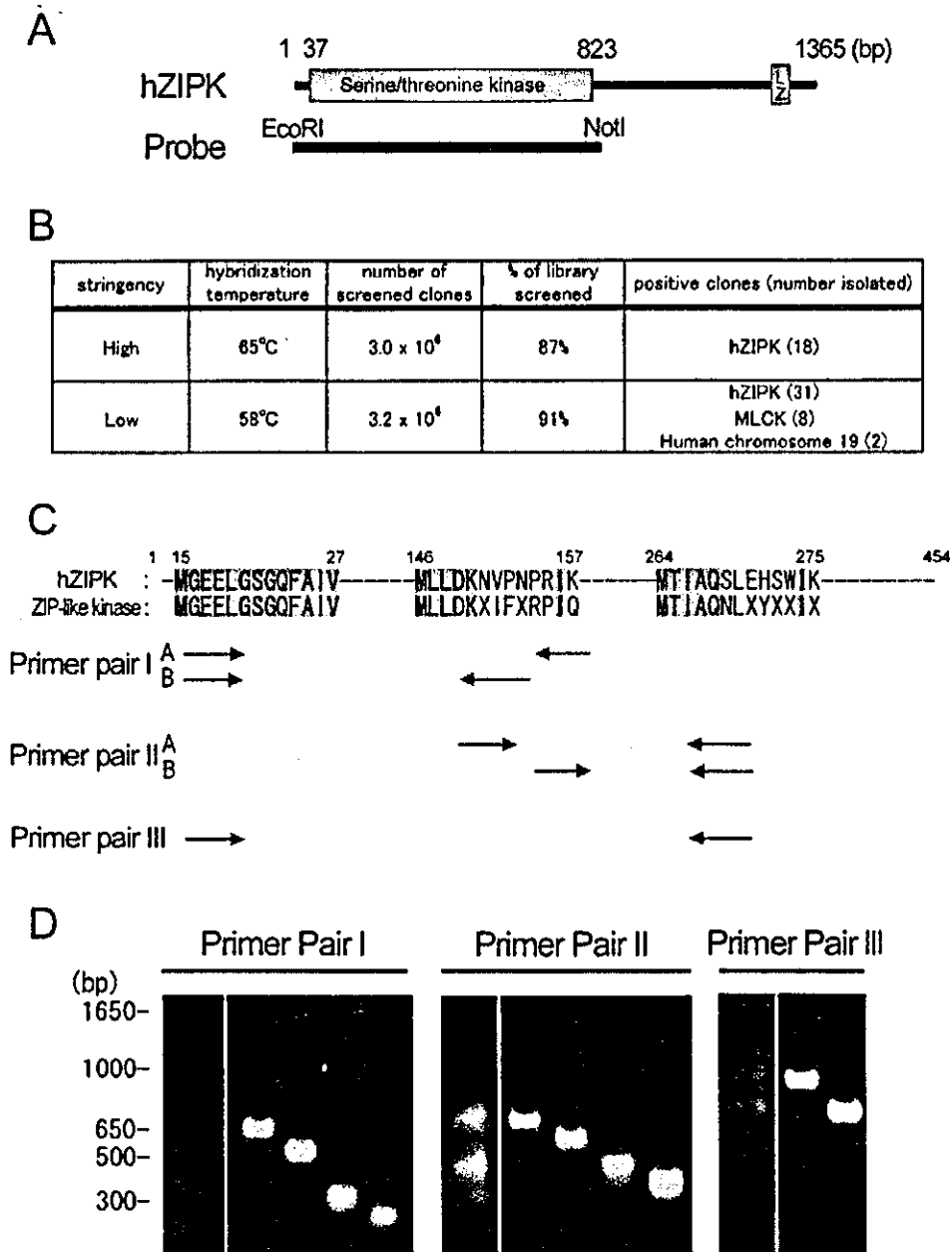


FIG. 2. Cloning of human ZIPK and related kinases from the human aortic vascular cDNA library. *A*, diagram of EcoRI-NotI fragments encoding the N-terminal kinase domain of ZIPK used as the probe to screen the human aortic cDNA library at both low and high stringency. Probe design was based on the previous report of homology between peptide fragments of ZIP-like kinase and the amino-terminal kinase domain of ZIPK (16). *B*, summary of clones isolated from the cDNA library screen with both low and high stringency hybridization conditions. *C*, degenerate PCR Studies to detect ZIP Kinase and ZIP-like kinase. Amino acid sequences of peptides derived from the putative ZIP-like kinase (16) and aligned with the amino acid sequence of hZIPK (GenBank™ accession number AB022341) are shown. Degenerate PCR primers corresponding to these amino acid sequences were designed (arrows) and used in PCR reactions with the human aorta library DNA as the template. The PCR products of primer pair IA and IIA shown were used as templates for PCR reactions with primer pair IB and IIB, respectively. *D*, PCR products of primer pair IB and IIB, as well as primer pair III, were size-fractionated by agarose gel electrophoresis (shown in the far left lanes in each panel). Four fragments from primer pair I and II and two fragments from primer pair III were gel-extracted and reamplified and are shown in the right section of the gel for each primer pair. The reamplified fragments were used for DNA sequencing. All cDNA recovered proved to be nonspecific, and no sequences corresponding to hZIPK or ZIP-like kinase were detected.

full-length ZIPK and N-terminal ZIPK both bound MBS, whereas GST-C-terminal ZIPK did not, supporting the idea that the amino-terminal half of ZIPK binds to MBS (Fig. 5D). Next, MBS and hZIPK were each immunoprecipitated from cells to test for an interaction between the two proteins *in vivo*. When MBS was immunoprecipitated from HEK293 cells, FLAG-hZIPK was present in the immunopellet (Fig. 6A), and,

reciprocally, the immunoprecipitation of FLAG-hZIPK led to the recovery of MBS in the immunopellet (Fig. 6B). These data indicate that hZIPK and MBS are complexed in the cell. Finally, we studied whether the small GTPase RhoA might regulate the interaction we observed between hZIPK and MBS. In GST pull-down assay studies, no differences were detected in the level of ZIP kinase bound by MBS from native Rho with

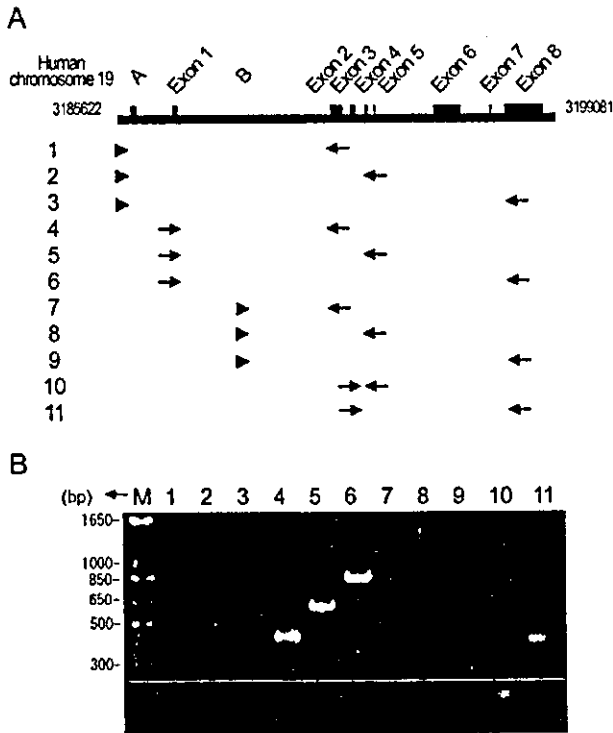


FIG. 3. Investigation of potential mRNA splice variants of human ZIP kinase. A, structure of the hZIPK gene on chromosome 19. The two predicted exons are labeled A and B. Exons 1, 2, 3, 4, 5, 6, 7, and 8 each encode 1-62, 63-423, 424-553, 554-603, 604-629, 630-783, 784-829, and 830-1365 bp of ZIP kinase, respectively. Each PCR primer was designed to correspond to each exon and predicted exon using the NCBI LocusLink program. *Arrows* indicate the forward and reverse primers corresponding to known exons; *arrowheads* indicate the forward primer corresponding to predicted potential exons A and B. B, PCR products were size-fractionated by agarose gel electrophoresis. A large number of DNA fragments amplified with this approach were sequenced; all sequences proved to be identical to hZIPK. M, 1-kb DNA ladder marker.

either RhoN19 (dominant negative) or RhoQL (constitutively active) (data not shown). MLC phosphorylation by ZIP kinase also was assayed by isolating ZIP kinase from cells expressing wild type Rho, RhoN19, or RhoQL, but differences in the level of MLC phosphorylation were not detected in this assay (data not shown). When hZIPK was immunoprecipitated, however, co-immunoprecipitation of MBS was significantly diminished in the presence of a dominant negative mutant of RhoA, RhoN19 (Fig. 7). The constitutively active Rho protein, RhoQL, did not increase the level of ZIPK bound to MBS above the level seen with native (wild type) Rho in these studies (Fig. 7). These immunoprecipitation data support the belief that active Rho promotes the hZIPK-MBS interaction characterized in these studies.

DISCUSSION

Because the regulatory pathways that modulate SMPP-1M activity remain incompletely understood, we undertook this study to identify the endogenous SMPP-1M-associated kinase(s). A 32-kDa ZIP-like kinase had been found previously to co-purify with and inhibit SMPP-1M activity, whereas 52-kDa hZIPK had been shown to phosphorylate MLC and cause cell contraction (16, 22, 25). We set out to clone the SMPP-1M-associated ZIP-like kinase from vascular tissue, employing two methods to screen a highly representative human aorta cDNA library for evidence of ZIP-like kinase. In the first approach, we performed colony hybridization using a probe against the 5'-

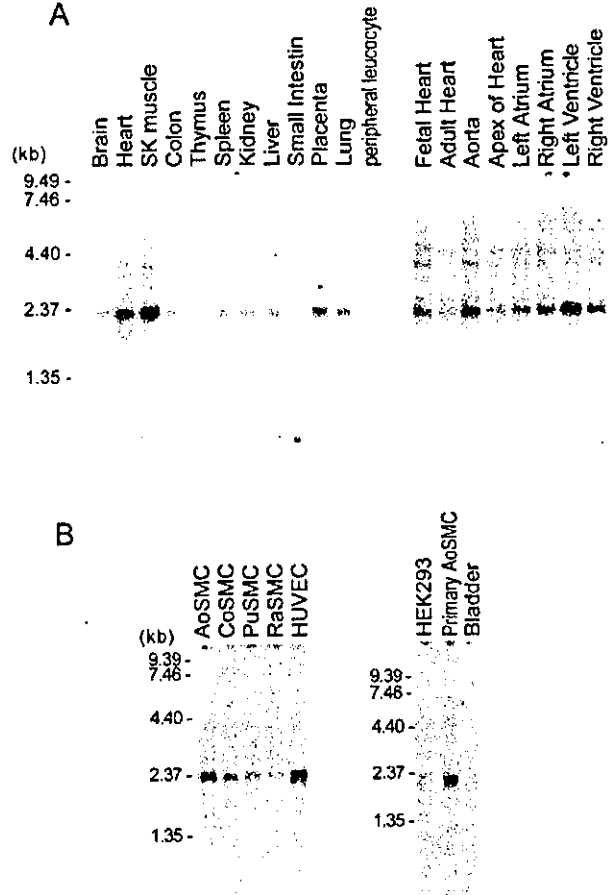


FIG. 4. Northern blotting studies of hZIPK mRNA expression in non-vascular and vascular tissues. A, multi-tissue Northern filters (Clontech). These filters, along with 1.5 μ g of poly(A)⁺ RNA from various human tissues, were hybridized with the radiolabeled 5'-end of hZIPK and exposed to a PhosphorImager (Amersham Biosciences). B, Northern filters prepared from human primary vascular cell lines and human bladder tissue RNA. Poly(A)⁺ RNAs (2 μ g) from various cultured cells and human bladder were loaded in each lane. The filters were hybridized with the radiolabeled 5'-end of hZIPK as a probe and exposed to a PhosphorImager. AoSMC, primary human aortic smooth muscle cell; CoSMC, human coronary arterial smooth muscle cell; PuSMC, human pulmonary arterial smooth muscle cell; RaSMC, human radial artery smooth muscle cell; HUVEC, human umbilical vein endothelial cells.

half of hZIPK, which, because of high homology, would be expected to identify both ZIP-like kinase and hZIPK. We also used a reverse transcription PCR approach with this human aorta library as the template and both degenerate primers and primers designed to identify hZIPK splice variants. In our studies, only hZIPK but not any ZIP-like kinase was present in this library.

As alternative approaches, we also used both the 5'-catalytic domain and full-length hZIPK as probes in both vascular and non-vascular cellular RNA Northern hybridization experiments. A variety of human tissues as well as human blood vessel, heart, and VSMCs from a variety of human blood vessel types were studied. Importantly, human bladder tissue was also studied because the ZIP-like kinase was originally purified from bladder smooth muscle tissue (16). In all of these tissues and cells only a single transcript of the expected 2.4 kb for hZIPK was detectable, supporting further the proposal that hZIPK is the sole SMPP-1 M-associated kinase expressed in human tissues.

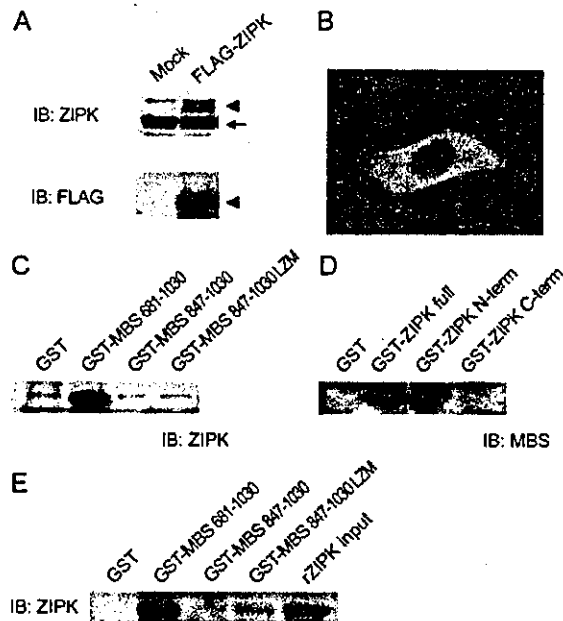


FIG. 5. Interaction of ZIPK with MBS *in vitro*. A, HEK293 cells were transfected with hZIPK plasmid or control plasmid, and cell lysates were immunoblotted (IB) with either anti-ZIPK (top) or anti-FLAG (bottom) antibodies. The arrow and arrowheads indicate endogenous hZIPK and FLAG-tagged hZIPK, respectively. B, HEK293 cells transiently transfected with hZIPK were fixed and stained with anti-FLAG antibody and visualized with immunofluorescence microscopy. Note that ZIP kinase is distributed uniformly throughout the cytoplasm in these cells. C, HEK293 cells transfected with hZIPK were lysed, and the lysates were then used in GST pull-down protein-protein interaction studies. Binding of ZIPK was probed using anti-FLAG antibody. The lane marked GST represents GST alone. GST-MBS constructs expressing either aa 681-1030 or aa 847-1030 are represented by the lanes marked GST-MBS 681-1030 or GST-MBS 847-1030. The lane marked GST-MBS 847-1030 L2M represents the construct expressing the domain of MBS with the leucine residues in the leucine zipper of the domain mutated to alanines. D, HEK293 cells transfected with hZIPK were lysed, and the lysates were then used in GST pull-down protein-protein interaction studies. GST, GST alone; GST-ZIPK Full, full-length ZIP kinase; GST-ZIPK N-term, N-terminal ZIP kinase with aa 1-288; GST-ZIPK C-term, C-terminal ZIP kinase with aa 288-454. E, human aortic vascular smooth muscle cells were lysed, and the lysates were then used in GST pull-down protein-protein interaction studies. Binding of ZIPK was probed using the anti-ZIPK antibody. The lane marked GST represents GST alone. GST-MBS constructs expressing either aa 681-1030 or aa 847-1030 are represented by the lanes marked GST-MBS 681-1030 or GST-MBS 847-1030. The lane marked GST-MBS 847-1030 L2M represents the construct expressing the domain of MBS with the leucine residues in the leucine zipper of the domain mutated to alanines (14). The far right lane shows a recombinant ZIPK (*rZIPK*) positive control.

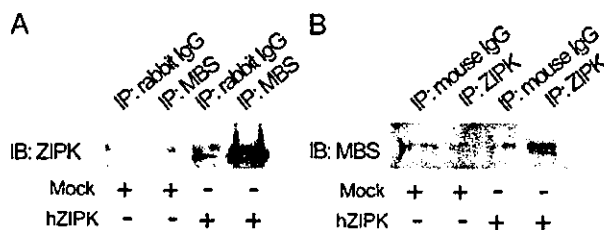


FIG. 6. Interaction of ZIPK with MBS in cells. HEK293 cells transfected with hZIPK were lysed, and lysates were then used in immunoprecipitation (IP) studies of human MBS (panel A) or ZIPK (panel B), followed by immunoblotting (IB) of ZIPK or MBS, respectively.

We also tested for the binding of hZIPK to MBS in several ways. Heterologous expression of hZIPK demonstrated that hZIPK binds directly to the coiled coil-containing domain of

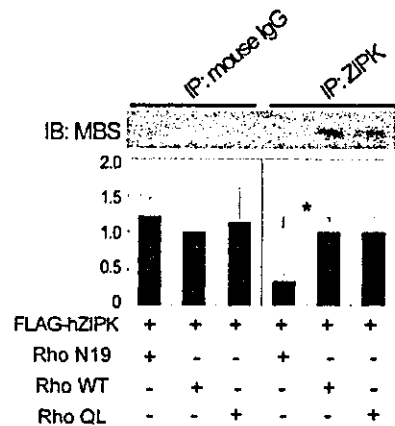


FIG. 7. Effect of small GTPase RhoA on the interaction between human ZIPK and MBS. HEK293 cells were cotransfected with hZIPK and wild type (WT) RhoA or either dominant negative (N19) or constitutively active (QL) RhoA. Immunoprecipitation (IP) with normal mouse IgG (control; left) or anti-FLAG antibody for ZIP kinase (right) was followed by immunoblotting (IB) with anti-MBS antibody and densitometric quantitation. The signal intensity of Rho wild type (Rho WT) was arbitrarily designated as unity. *, $p < 0.01$ ($n = 3$ to 5).

MBS in GST pull-down protein-protein interaction studies and to complexes with MBS in co-immunoprecipitation experiments, strongly supporting the idea that hZIPK interacts with MBS in the cell. Furthermore, disruption of RhoA activation by overexpression of a dominant negative RhoA mutant inhibited this hZIPK-MBS interaction in cells. We did not detect an effect of RhoN19 on hZIPK-MBS binding using GST fusion proteins or in a MLC phosphorylation assay using immunoprecipitated hZIPK derived from cells expressing wild type or mutant Rho protein. These negative data support either the reduced sensitivity of these assays compared with co-immunoprecipitation or the need for additional cellular proteins for Rho to regulate the hZIPK-MBS interaction. Taken together, the data support the hypothesis that the interaction between hZIPK and MBS may be regulated by RhoA and that hZIPK may play a role in PP1M regulation by RhoA.

Studies in both animals and humans have shown that SMPP-1M activity is regulated in health and in disease. Hyperactivity of the RhoA pathway leading to SMPP-1M inhibition and blood vessel contraction has been shown in hypertensive states, and enzyme inhibitors that prevent SMPP-1M inhibition are promising new treatments for cardiovascular disorders (26, 27). Our data establish that hZIPK is the SMPP-1M-associated kinase and support the hypothesis that the hZIPK-SMPP-1M interaction is regulated by RhoA. Future studies will be directed at defining the role of hZIPK in the modulation of SMPP-1M activity by vasoconstrictor agonists and other potential mechanisms through which hZIPK regulates vascular smooth muscle cell function.

REFERENCES

- Hartshorne, D. J. (1987) in *Physiology of the Gastrointestinal Tract* (Johnson, D. R., ed) pp. 423-482, Raven Press, Ltd., New York
- Somlyo, A. P., and Somlyo, A. V. (1994) *Nature* 372, 231-236
- Alessi, D., MacDougall, L. K., Sola, M. M., Ikebe, M., and Cohen, P. (1992) *Eur. J. Biochem.* 210, 1023-1035
- Surks, H. K., Mochizuki, N., Kasai, Y., Georgescu, S. P., Tang, K. M., Ito, M., Lincoln, T. M., and Mendelsohn, M. E. (1999) *Science* 286, 1583-1587
- Khatri, J. J., Joyce, K. M., Brozovich, F. V., and Fisher, S. A. (2001) *J. Biol. Chem.* 276, 37250-37257
- Eiter, E. F., Eto, M., Wardle, R. L., Brautigam, D. L., and Murphy, R. A. (2001) *J. Biol. Chem.* 276, 34681-34685
- Lee, M. R., Li, L., and Kitazawa, T. (1997) *J. Biol. Chem.* 272, 5063-5068
- Wu, X., Somlyo, A. V., and Somlyo, A. P. (1996) *Biochem. Biophys. Res. Com.* 220, 658-663
- Kamm, K. E., and Stull, J. T. (1985) *Annu. Rev. Pharmacol. Toxicol.* 25, 593-620
- Taylor, D. A., and Stull, J. T. (1988) *J. Biol. Chem.* 263, 14456-14462

11. Eto, M., Senba, S., Morita, F., and Yazawa, M. (1997) *FEBS Lett.* **410**, 356–360
12. Eto, M., Kitazawa, T., Yazawa, M., Mukai, H., Ono, Y., and Brautigan, D. L. (2001) *J. Biol. Chem.* **276**, 29072–29078
13. Kimura, K., Ito, M., Anano, M., Chihara, K., Fukata, Y., Nakafuku, M., Yamamori, B., Feng, J., Nakano, T., Okawa, K., Iwamatsu, A., and Kaibuchi, K. (1996) *Science* **273**, 245–248
14. Surks, H. K., Richards, C. T., and Mendelsohn, M. F. (2003) *J. Biol. Chem.* **278**, 51484–51493
15. Trinkle-Mulcahy, L., Ichikawa, K., Hartshorne, D. J., Siegman, M. J., and Butler, T. M. (1995) *J. Biol. Chem.* **270**, 18191–18194
16. MacDonald, J. A., Borman, M. A., Muranyi, A., Somlyo, A. V., Hartshorne, D. J., and Haystead, T. A. J. (2001) *Proc. Natl. Acad. Sci. U. S. A.* **98**, 2419–2424
17. Muranyi, A., MacDonald, J. A., Deng, J. T., Wilson, D. P., Haystead, T. A., Walsh, M. P., Erdodi, F., Kiss, E., Wu, Y., and Hartshorne, D. J. (2002) *Biochem. J.* **366**, 211–216
18. Muranyi, A., Zhang, R., Liu, F., Hirano, K., Ito, M., Epstein, H. F., and Hartshorne, D. J. (2001) *FEBS Lett.* **493**, 80–84
19. Broustas, C. G., Grammatikakis, N., Eto, M., Dent, P., Brautigan, D. L., and Kasid, U. (2002) *J. Biol. Chem.* **277**, 3053–3059
20. Borman, M. A., MacDonald, J. A., Muranyi, A., Hartshorne, D. J., and Haystead, T. A. (2002) *J. Biol. Chem.* **277**, 23441–23446
21. Kawai, T., Matsumoto, M., Takeda, K., Sanjo, H., and Akira, S. (1998) *Mol. Cell. Biol.* **18**, 1642–1651
22. Niiro, N., and Ikebe, M. (2001) *J. Biol. Chem.* **276**, 29567–29574
23. Ichiba, T., Hashimoto, Y., Nakaya, M., Kuraishi, Y., Tanaka, S., Kurata, T., Mochizuki, N., and Matsuda, M. (1999) *J. Biol. Chem.* **274**, 14376–14381
24. Crunstein, M., and Hogness, D. S. (1975) *Proc. Natl. Acad. Sci. U. S. A.* **72**, 3961–3965
25. Murata-Hori, M., Suizu, F., Iwasaki, T., Kikuchi, A., and Hosoya, H. (1999) *FEBS Lett.* **451**, 81–84
26. Uehata, M., Ishizaki, T., Satoh, H., Ono, T., Kawahara, T., Morishita, T., Tamakawa, H., Yamagami, K., Inui, J., Maekawa, M., and Narumiya, S. (1997) *Nature* **389**, 990–994
27. Kandabashi, T., Shimokawa, H., Mukai, Y., Matoba, T., Kunihiro, I., Morikawa, K., Ito, M., Takahashi, S., Kaibuchi, K., and Takeshita, A. (2002) *Arterioscler. Thromb. Vasc. Biol.* **22**, 243–248

Transmission of Force and Displacement within the Myosin Molecule[†]Takashi Ohki,[‡] Sergey V. Mikhailenko,[‡] Manuel F. Morales,[§] Hirofumi Onishi,^{*,‡} and Naoki Mochizuki[‡]*Department of Structural Analysis, National Cardiovascular Center Research Institute, Fujishiro-dai, Suita, Osaka 565-8565, Japan, and University of the Pacific, San Francisco, California 94115**Received May 23, 2004; Revised Manuscript Received August 14, 2004*

ABSTRACT: Myosin is a repetitive impeller of actin, using its catalysis of ATP hydrolysis to derive repeatedly the required free energy decrements. In each impulsion, changes at the myosin active site are transmitted through a series of structural elements to the myosin propeller (lever arm), almost 5 nm away. While the nature of transmission through most elements is evident, that through the so-called converter is not. To investigate how the converter changes linear displacement into rotation, we tested (one at a time) the effect of two Phe residue mutations (at 721 and 775) in the converter on the overall function of a heavy meromyosin (or subfragment 1) system, after first showing by observing kinetic behaviors that neither mutation affects other elements in the transmission. Using three tests (direct movement of the lever arm, activity in a motility assay with actin filaments, and direct force measurement of lever arm function), we found that these mutations affected only movements of the converter and the lever arm. From interpreting our observations in terms of the structure of the converter, we deduce that the linear–rotational transformation in the converter is mediated by a little machine (two Phe residues linked to a Gly) within a machine.

Myosin is the enzyme that catalyzes the hydrolysis of ATP, liberating the free energy used for the actin-propelling work in muscle contraction (1, 2). But now, at the scale that can be accessed by X-ray crystallography and electron microscopy, myosin is seen as a complicated machine of many moving parts (3–9). Its catalytic function (conducted at its active site) is a long distance from the site of its actin propeller (lever arm) (5, 6). Intervening are the relay helix and a poorly understood structure called the converter (7, 8). When hydrolysis at the active site is transduced into force and displacement, these effects are transmitted by the intervening elements to the lever arm (7, 8). Our aim is to understand how the overall transmission is accomplished, so we have to determine how the converter works. To get at this, we alter the converter structure by two especially chosen site-directed mutations, and draw inferences from what we observe. However, what we observe (changes in the movement of the lever arm resulting from a mutation) is meaningful only if we are sure that the mutation alters the converter element alone. Logically, we must begin with evidence that this is true.

The chemical kinetics describing the changes undergone by a myosin system are aptly described by the differential equation of Bagshaw and Trentham (B–T) (10, 11). The equation tracks in time, t , the linear succession of the predominant myosin species, $M_i(t)$, as the enzyme binds the

substrate and changes conformation, etc., and later as it sheds first the inorganic phosphate (P_i) and then ADP. Elsewhere, we (12, 13) and others (14, 15) show why the early stages in this succession report transformations at, or near, the active site, and then remote effects on the relay helix. Toward the end of ATP degradation, the stages report the $M_i(t)$ during the release of products, P_i and ADP. Once the numerical values of the rate constants of the equation are known, the equation allows the complete simulation of the degradation, or, if one wishes, of its early and late phases.

With this prospect in mind, three heavy meromyosin (HMM)¹ systems are prepared. One is normal (wild-type) HMM, and the others are the special mutants, in which Phe residues at positions 721 and 775 are replaced with Ala (F721A and F775A, respectively). It is known that both altered positions are located within the converter (7). With each system, standard experiments are performed to obtain the matrix of B–T rate constants, wherein some constants alone describe the early and some the late stages of ATP degradation. By comparing the kinetic data from the wild-type and mutant systems, we find that these particular mutations do not matter in the early events involving the active site or the relay helix, and also that they do not matter in the late events of ATP degradation. These findings warrant the conclusion that when performance tests of transmission detect any differences upon mutation, the differences are, most likely, effects on the converter, not adventitious effects on other elements of the system. Next, using three performance tests of transmission, we show that the test scores

[†] Supported by grants from the Ministry of Education, Culture, Sports, Science and Technology (to H.O. and N.M.), from the Ministry of Health, Labour and Welfare (to N.M.), and from the National Science Foundation (to M.F.M.).

* To whom correspondence should be addressed. Telephone: +81-6-6833-5012. Fax: +81-6-6872-8092. E-mail: honishi@ri.ncvc.go.jp.

[‡] National Cardiovascular Center Research Institute.

[§] University of the Pacific.

¹ Abbreviations: HMM, heavy meromyosin; S1, subfragment 1; mant-ATP, 2'(3')-O-(N-methylanthraniloyl)adenosine 5'-triphosphate; RLC, regulatory light chain; ELC, essential light chain; CFP, cyan fluorescent protein; YFP, yellow fluorescent protein.

differ greatly in the middle phase involving the converter. After understanding the detailed structure of the converter, we work back by model building to understand how nucleotide binding, cleft closure, and subsequent events are connected with the converter, and thus, we obtain an overview of the transmission process (in the Discussion).

MATERIALS AND METHODS

Preparation of Recombinant HMMs and S1s. A chicken smooth-muscle myosin heavy chain cDNA clone was supplied by T. Masaki (16). A baculovirus transfer vector for wild-type HMM, with the His tag sequence at its N-terminal end and the myc tag sequence at its C-terminal end, in pFastBacHTa (Clontech, Palo Alto, CA), was produced as described previously (17). Site-directed mutagenesis was carried out using Kunkel's method (18) to replace Phe-721 or Phe-775 in the heavy chain sequence with alanine residues.

The cDNA for yellow fluorescent protein (YFP) was amplified from pEYFP-C1 (Clontech, Palo Alto, CA) by the polymerase chain reaction (PCR), creating an *Afl*III site at its N-terminus and an *Nco*I site at its C-terminus. The PCR product was digested with *Afl*III and *Nco*I, and subcloned into pFastBacHTa (named pFastBacHT-YFP). A transfer vector for the full-length sequence of the YFP-fused subfragment 1 (S1) heavy chain was prepared as described previously (19), but with pFastBacHT-YFP instead of pFastBacHTa.

The cDNA for cyan fluorescent protein (CFP) was amplified from pECFP-C1 (Clontech) by PCR with the same primers that were used in amplifying YFP. The PCR product was digested with *Afl*III and *Nco*I, and subcloned into pFastBacNN (19) (named pFastBacNN-CFP). pG17-1, which was plasmid pUC118 encoding the myosin essential light chain (ELC) and including a unique *Afl*III site at its initiating methionine codon (20), was digested with *Afl*III and *Pst*I, and subcloned into pFastBacNN-CFP. pRLCA, which was plasmid pUC119 encoding the myosin regulatory light chain (RLC) (20), was digested with *Afl*III and *Eco*RI, and subcloned into pFastBacNN. A *Bst*1107I site was created at the unique *Avr*II site of the transfer vector and was then digested with *Bst*1107I. To make a transfer vector for both myosin light chains, a cDNA fragment containing the coding region of the RLC was ligated into the *Bst*1107I site of the transfer vector containing the CFP-fused ELC sequence.

Expression and purification of wild-type and mutant HMMs were carried out as described previously (17). Chimeric S1s (named C/Y-S1), in which YFP was fused to the N-terminus of the S1 heavy chain and CFP was fused to the N-terminus of the ELC, were prepared by essentially the same method that was used for preparing recombinant S1s (19).

Stopped-Flow Experiments. Stopped-flow experiments were performed using an SF61-DX2 stopped-flow spectrophotometer (Hi-Tech Scientific, Salisbury, U.K.) with a 75 W Xe/Hg lamp, as described previously (12).

Fluorescence Measurements. Steady-state fluorescence was measured using an F-4500 fluorescence spectrophotometer (Hitachi, Tokyo, Japan). CFP (donor) was excited at 433 nm, and its emitted spectra were recorded from 450 to 600 nm. Efficiencies (E) were calculated from donor fluorescence quenching at 475 nm as $1 - F_{DA}/F_D$, where

F_{DA} is the fluorescence of the C/Y-S1 and F_D is the fluorescence of S1 fused by CFP only. CFP and YFP were treated as point masses. The distance between CFP and YFP fluorophores was calculated using the Förster equation (21, 22), where $R = R_0(1/E - 1)^{1/6}$. The Förster distance, R_0 , was calculated as $R_0 = (8.8 \times 10^{-23})(Q_D \kappa^2 n^{-4} J)^{1/6}$, where J is the overlap integral between CFP and YFP attached to the S1 expressed in $M^{-1} \text{ cm}^3$ ($J = 2.18 \times 10^{-13}$), κ^2 is the orientation factor (assumed to be 0.667), n is the refractive index (assumed to be 1.4), and Q_D is the quantum yield (0.4 for CFP) obtained from the manufacturer's manual (Clontech). The calculated R_0 was 4.86 nm.

In Vitro Motility Assay. A motility assay was performed as described previously (17). Briefly, after the RLC was phosphorylated by myosin light chain kinase, myc-tagged HMMs were allowed to bind to the nitrocellulose-coated glass surface of the flow cell by using a monoclonal antibody against c-myc (9E10, Pharmingen, San Diego, CA); 8 μL of the concentrated antibody solution (0.3 mg/mL) was used to create a dense HMM surface, and 8 μL of the diluted solution (0.075 mg/mL) was used to create a sparse HMM surface. Actin filaments labeled with rhodamine phalloidin were infused into the flow cell, and the sliding movement of actin filaments in the presence of ATP was observed using an epifluorescence inverted IX70 microscope (Olympus, Tokyo, Japan) equipped with a rhodamine filter set.

Optical Tweezers and Nanometry. We used an inverted fluorescence IX71 microscope (Olympus) equipped with optical tweezers (Sigma Koki, Tokyo, Japan) and a quadrant photodetector (Sentech, Osaka, Japan) (23, 24). Optical tweezers were used to independently control two polystyrene beads. Experiments were performed in a flow cell made from two parallel coverslips. Polystyrene beads (2 μm) were decorated sparsely with myc-tagged phosphorylated HMMs using anti-c-myc antibody. The beads were allowed to bind to the nitrocellulose-coated coverslip surface in a solution containing 25 mM KCl, 5 mM MgCl_2 , and 20 mM HEPES (pH 7.8). The solution was replaced with one containing rhodamine phalloidin-labeled actin filaments and 1 μm polystyrene beads that had been precoated with α -actinin. A single actin filament was attached at either end to a bead held in the optical tweezers. Interactions between actin and the surface-bound HMM were monitored by projecting the image of one of the beads onto the center of a quadrant photodetector after enlarging it 10^3 times. In the assay, the solution was supplemented with 1–10 μM ATP, 0.5% (v/v) 2-mercaptoethanol, and an oxygen-scavenger system (glucose oxidase, catalase, and glucose). The stiffness of the laser trap was calculated from the variance of the Brownian motion of the trapped bead, using the equipartition law, $\frac{1}{2}K\langle X^2 \rangle = \frac{1}{2}K_b T$, where K is stiffness, $\langle X^2 \rangle$ is the standard deviation of the bead position, K_b is Boltzmann's constant, and T is temperature.

RESULTS

Mutations Do Not Significantly Affect the Early or Late States of ATP Hydrolysis. The question of whether a perturbation affects the very early stages of the myosin process is best answered by comparing the performance of a mutated system with the wild-type system, focusing on the early rate constants that characterize each system. The

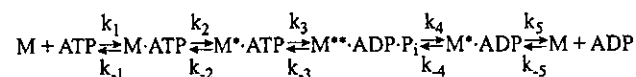
Table 1: Rate Constants and Extents of Interaction with Nucleotides and Actin in Wild-Type and Mutant HMMs

	parameter	wild type	F721A	F775A
mant-ATP binding ^a	increase (%)	100	104	104
	K_1k_2 ($s^{-1} M^{-1}$)	3.3×10^5	3.3×10^5	3.2×10^5
Trp fluorescence ^a	increase (%)	18	14	13
	K_1k_2 ($s^{-1} M^{-1}$)	2.7×10^5	1.9×10^5	2.1×10^5
	k_{max} (s^{-1})	230	large	130
	$K_{0.5}$ (mM)	1	large	0.7
mant-ADP release ^a	k_5 (s^{-1})	1.3	1.5	1
	k_{cat} (s^{-1})	0.023 ± 0.001	0.058 ± 0.010	0.043 ± 0.001
basic ATPase ^b	V_{max} (s^{-1})	2.1 ± 0.3	0.71 ± 0.02	2.0 ± 0.1
	K_{actin} (mM)	0.050 ± 0.012	0.043 ± 0.004	0.053 ± 0.007

^a Conditions: 0.45 M KCl, 2 mM MgCl₂, and 20 mM Tris-HCl (pH 7.5) at 20 °C. ^b Conditions: 0.45 M KCl, 2 mM MgCl₂, and 20 mM Tris-HCl (pH 7.5) at 25 °C. ^c Conditions: 0.01 M KCl, 2 mM MgCl₂, and 20 mM Tris-HCl (pH 7.5) at 25 °C.

constants are given as k_i , k_{-i} , and K_i ($i = 1, 2, \dots$) in the B-T chemical kinetic scheme (10, 11) (Scheme 1²).

Scheme 1



The constants for the first process were experimentally measured using 2'(3')-O-(N-methylanthraniloyl)adenosine 5'-triphosphate (mant-ATP) (25) in place of ATP so that the occupation of the active site can be inferred from the fluorescence emitted by the bound mant-ATP. Using mutant systems, addition of excess mant-ATP produced essentially the same increases in fluorescence that the wild-type system did (Table 1). The second-order rate constants (K_1k_2), estimated from the slope of the plots of the observed rate constant (k_{obs}) versus mant-ATP concentration, were very similar in the wild-type and mutant systems (Table 1). The second process, which was the conversion of $M \cdot ATP$ to $M^* \cdot ATP$, was measured directly in the three systems using the fact that Trp-512, located at the distal tip of the relay helix within the motor domain (6), enhances its fluorescence when the influence traveling from the active site reaches the helix (15, 26, 27). Upon addition of excess ATP, the increase in the Trp fluorescence for the mutant systems was only slightly smaller than that in the wild-type system (Table 1). Time transients of the fluorescence increase could be well fitted by a single exponential. The k_{obs} values were linearly dependent on ATP concentration at low ATP concentrations. The K_1k_2 values for the mutant systems were similar to those estimated from the development of mant fluorescence and close to the K_1k_2 value obtained for the wild-type system (Table 1).

However, the k_{obs} values were no longer linearly dependent on ATP concentration at greater ATP concentrations, in which range the dependence became quasi-hyperbolic [$k_{obs} \approx k_{max}[ATP]/([ATP] + K_{0.5})$]. In the wild-type system, it is known that k_{max} corresponds to the rate of the hydrolytic transition (process 3 in the B-T sequence) (28). In the F775A system, the values of both k_{max} and $K_{0.5}$ were similar to those of the wild-type system; however, these parameters

were too large to be measured in the F721A system (Table 1). It will be shown later that the mechanical linkage between the SH1 helix and the converter is completely disrupted in the F721A system. Normally, the acceleration of movement of the relay helix is slowed by the mass of the lever arm linked to the relay helix via the converter. We therefore may speculate that the large value of $k_3 + k_{-3}$ for the F721A system is the result of the faster movement of its relay helix, which is unregulated by the mass of the converter-lever arm system. We conclude that neither of our two perturbations significantly affects the events leading up to the arrival of the influence at the converter.

We also investigated whether the perturbations affected the two slow transitions (processes 4 and 5 in the B-T sequence) by measuring in each of the three systems the steady-state ATPase activity, and the rate of displacement of mant-ADP from the HMM-mant-ADP complex with excess ATP. The ATPase activities (k_{cat}) and the displacement rates (k_5) were similar in all three systems (Table 1). Moreover, it is interesting to note that the mutated systems exhibit actin activation (V_{max}) similar to that of the wild-type system (although F721A shows slightly lower levels), and that the K_{actin} values are also similar (Table 1). Together, the foregoing results show that the perturbations to be described next are specific effects produced on the converter, and not on any other element in the sequence.

Mutations Affect Movements of the Converter and the Lever Arm. For the first performance test of whether the mutations affect the lever arm movement, we constructed a test device, a chimeric S1³ (C/Y-S1) in which YFP is fused to the N-terminus of the S1 heavy chain and CFP is fused to the N-terminus of the ELC. Because the CFP-to-YFP energy transfer between these fluorophores is well-understood and depends selectively on the distance between them, it is possible to detect their separation using optical measurements alone (21, 29). Excitation of CFP at 433 nm resulted in a cyan emission at 450–515 nm, and the fluorescence energy transfer resulted in a yellow emission at 515–600 nm. When ATP or ADP was added to the wild-type C/Y-S1, the cyan emission from CFP decreased while the yellow emission from YFP increased (Figure 1A). The distance between the fluorophores decreased from 7.4 to 6.2 nm upon addition of ATP, and to 6.9 nm upon addition of ADP (Table 2). The distance between the termini, which was estimated

² In chemical notation, M stands for the truncated double-headed myosin that was used in our experiments, which is usually called HMM. Conformers of this protein, which can be distinguished by their absorbance or fluorescence, are denoted with one or two asterisks. As usual, k_i and k_{-i} are the forward and reverse rate constants, respectively of the i th reaction.

³ To simplify the system, the single head of myosin, which is called S1, was used in this experiment.

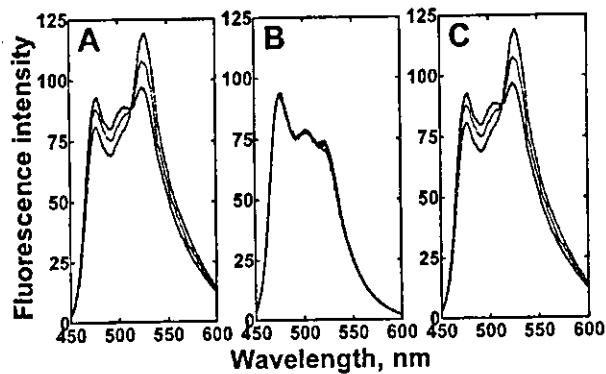


FIGURE 1: Fluorescence resonance energy transfer emission spectra. Emission spectra of wild-type (A), F721A (B), and F775A (C) C/Y-S1s excited at 433 nm were obtained in the absence of nucleotide (—), in the presence of 1 mM ATP (---), or in the presence of 0.1 mM ADP (···). Conditions: 0.1 μ M C/Y-S1s, 0.45 M KCl, 2 mM MgCl₂, 50 mM Tris-HCl (pH 8.0), and 0.5 mM dithiothreitol at 25 °C.

Table 2: Distances between CFP and YFP in Wild-Type and Mutant C/Y-S1s

C/Y-S1	nucleotide	FRET efficiency	distance (nm)
wild type	none	0.079 \pm 0.010	7.4 \pm 0.2
	ATP	0.183 \pm 0.012	6.2 \pm 0.1
	ADP	0.107 \pm 0.008	6.9 \pm 0.1
F721A	none	0.070 \pm 0.005	7.3 \pm 0.1
	ATP	0.082 \pm 0.007	7.4 \pm 0.1
	ADP	0.079 \pm 0.001	7.4 \pm 0.1
F775A	none	0.087 \pm 0.002	7.5 \pm 0.1
	ATP	0.201 \pm 0.014	6.1 \pm 0.1
	ADP	0.114 \pm 0.024	6.9 \pm 0.4

from the crystal structure of the motor domain complexed with an ATP analogue, was \sim 1.0 nm shorter than that estimated on the unligated motor domain (3, 7). Therefore, the movement observed using the CFP fluorophore correlates well with the movement of the lever arm. When either ATP or ADP was added to the F721A C/Y-S1, there was no change in the energy transfer between the fluorophores (Figure 1B and Table 2). However, when these additions were made to the F775A C/Y-S1, the energy transfer changed just as it did in the wild-type C/Y-S1 (Figure 1C and Table 2). These results indicate that when either the wild-type or the F775A system undergoes the transition from the M to the M** state (see Scheme 1), it swings its lever arm, whereas the F721A system does not.

While the previous test examined the movement that myosin uses in carrying out its functions, the next two sample what is presumably the teleological function of myosin. We tested the speed at which actin is propelled [using a motility assay (30, 31)], modulating the test severity by varying the resistance offered to its movement. On a surface that was densely covered with HMM molecules, the wild-type system propelled actin filaments at a speed of $0.51 \pm 0.05 \mu\text{m/s}$, but neither of the mutant systems moved actin filaments at all (Figure 2A). On a sparsely covered surface, the F721A system remained unable to propel actin filaments (Figure 2B). Surprisingly, however, we detected a slow movement of filaments by the F775A system (average velocity of $0.07 \mu\text{m/s}$) under these conditions (Figure 2B). This indicates that although the F775A mutant retains the ability to swing its lever arm, its motor function is very weak. Mixing equal amounts of either F721A or F775A and the wild-type system

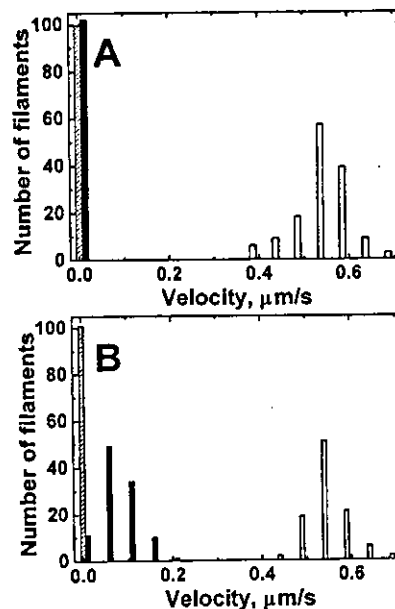


FIGURE 2: Distributions of the velocity of movement of actin filaments on glass surfaces densely (A) and sparsely (B) coated with HMMs: wild-type (empty), F721A (hatched), and F775A (filled). Conditions: 25 mM KCl, 3 mM MgCl₂, 20 mM HEPES (pH 7.8), and 2 mM ATP at 30 °C.

did not decrease the contribution of the wild-type component, indicating that the reduced motility expresses an inability of the mutant to generate force, but not irreversible binding of mutant dead heads to the actin filaments (data not shown).

In a final test of the wild-type and two mutated systems, we studied directly the ability of individual HMM molecules to exert force on actin. A single actin filament that was held taut by optical tweezers was brought close to a static bead that was sparsely coated with HMM molecules, and its position in space was sensitively monitored by projecting the bright-field image of the bead attached to the end of the actin filament onto a quadrant photodiode (23, 24). Using weak trapping forces, there was significant thermal motion, which was expressed as positional variance of the held bead, except when actin-HMM interactions occurred. The equilibrium position without interactions between actin and HMM was defined as zero displacement. Both the wild-type and mutant systems showed periods of such low variance (therefore high stiffness) in their records (Figure 3A-F). The distribution of bead positions during these periods was fitted to a Gaussian curve, and the shift of the curve peak from the zero displacement position was called the size of the power stroke (Figure 3G-L). Under moderate trapping forces (stiffness of 0.03 pN/nm per bead), the shifts for both mutant systems were nearly zero (Figure 3I,K), which was much less than that of the wild-type system ($6.5 \pm 0.6 \text{ nm}$, Figure 3G). This indicates that neither of the mutants exerted sufficient force to pull the bead after the interaction between actin and HMM occurred. Next, we attempted to detect the weaker forces by lowering the stiffness of each trap to 0.008 pN/nm per bead. Under these conditions, the F775A system was able to pull the bead, although its power stroke was somewhat smaller than that of the wild-type system (5.5 and 6.9 nm, respectively; panels L and H of Figure 3). However, the F721A system was still unable to displace the bead under these conditions, even when so weakly trapped (Figure 3J). Thus, the results of this direct measurement of force correlate

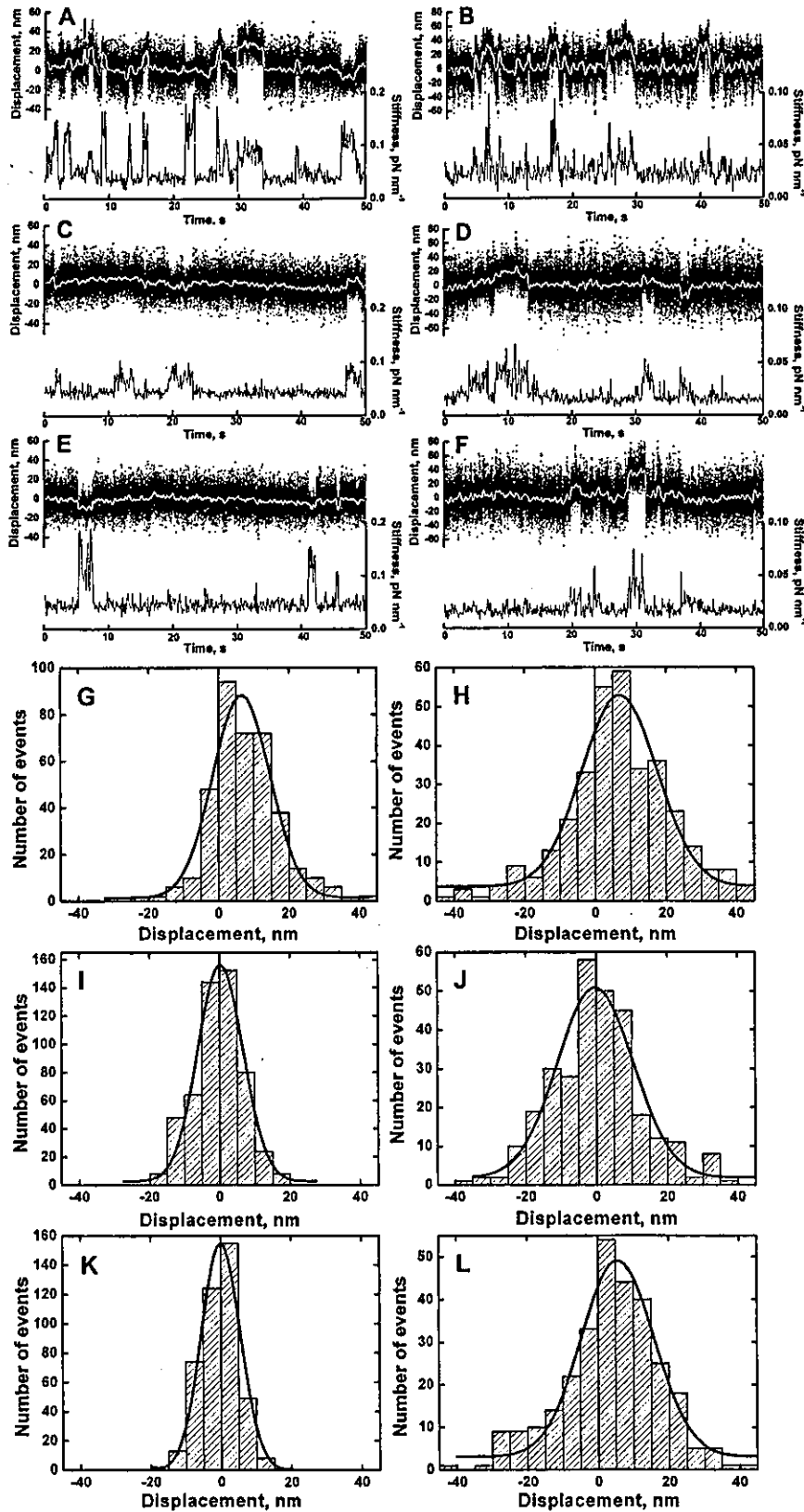


FIGURE 3: Displacements of actin filaments under moderately and extremely weak trapping forces caused by interactions with a single molecule of HMM. (A–F) In the data traces, the top traces show typical records of the displacements made by an HMM molecule at $1 \mu\text{M}$ ATP, the dots are raw data, the white lines are data passed through a low pass filter with a bandwidth of 2 Hz, and the bottom traces show stiffness calculated at intervals of 50 ms from the variance of the trapped bead position. (G–L) In the histograms of the displacements, solid vertical lines show the equilibrium (zero) position of the bead without interactions between actin and HMM. The fits to single Gaussian distributions are shown as solid lines. Mean sizes of the power stroke are 6.5 ± 0.6 nm for panel G, 6.9 ± 0.7 nm for panel H, 0.2 ± 0.4 nm for panel I, -0.4 ± 0.5 nm for panel J, -0.1 ± 0.4 nm for panel K, and 5.5 ± 0.7 nm for panel L. The trapping stiffness of each bead was 0.03 pN/nm for a moderately weak trapping force (A, C, E, G, I, and K) and 0.008 pN/nm for an extremely weak trapping force (B, D, F, H, J, and L). HMMs: wild-type (A, B, G, and H), F721A (C, D, I, and J), and F775A (E, F, K, and L). Conditions: 25 mM KCl, 5 mM MgCl_2 , 20 mM HEPES (pH 7.8), and 1 – $10 \mu\text{M}$ ATP at $\sim 20^\circ\text{C}$.

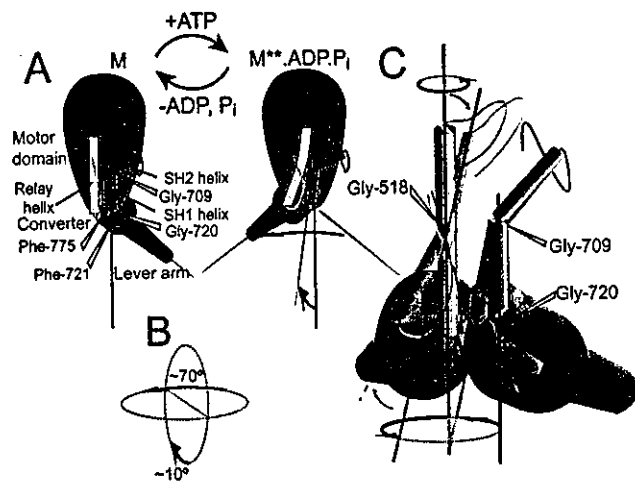


FIGURE 4: Mechanism by which motions within the motor domain are converted into a large rotation of the converter. (A) Lever arm swing. Myosin, initially in the M state (left), binds and rapidly hydrolyzes ATP to assume the metastable $M^{**}\cdot ADP\cdot P_i$ state (right). The relay helix and the SH1 (lower)/SH2 (upper) helices are shown as yellow and green rectangles, respectively. The ends of the relay helix are connected to the switch II loop (orange) and the converter (blue). The locations of Gly-709 (the flexible joint between the SH1 and SH2 helices), Gly-720 (the putative center for the rotation of the converter), and the two mutated residues (Phe-721 and Phe-775) are also shown. (B) ATP-induced conformational change, consisting of two almost perpendicular rotations. (C) Superimposition of nucleotide-free (the opaque image) and nucleotide-ligated (the translucent image) states. The converter and the lever arm are colored blue and purple, respectively. The switch II loop is shown as an orange strand, the relay loop as a silver strand, and the relay helix as a silver rod, and the SH1 (lower) and SH2 (upper) helices are shown as green rods. Arrows indicate the directions of shifts and rotations of the relay and SH1 helices that are induced by the closure of the nucleotide-binding cleft. The side chains of Phe-721 and Phe-775 are shown as red and pink hexagons, respectively. The β -sheet structure in the converter is shown as light-blue plane ribbons. The crystal structures of the skeletal muscle myosin with no nucleotide [Protein Data Bank (PDB) entry 2MYS] (3) and smooth muscle myosin complexed with $MgADP\cdot AlF_4^-$ (PDB entry 1BR4) (7) were adapted for the nucleotide-free and nucleotide-ligated myosin heads, respectively.

perfectly with those of the other performance tests (ability to swing the lever arm and to propel actin filaments in an *in vitro* motility assay), confirming that both mutations have special effects on the converter; the F775A mutation sharply inhibits its function but, unlike the F721A mutation, does not abolish it.

DISCUSSION

Since we can now refer to the three performance tests in Mutations Affect Movements of the Converter and the Lever Arm that report on the converter, we conclude that the two mutations had quite different effects on this element: the mutation at position 775 sharply inhibited its function, whereas the mutation at position 721 completely abolished it. We now describe the converter setting and its structure, and explain why these particular mutations were chosen. Thinking of the motor domain as fixed, we discuss the relative motion of the converter and the rigidly attached lever arm, focusing on the landmark of the SH1 helix (Figure 4A). The suggested movement of the converter when ATP is added to the distant active site is the sum of two almost perpendicular rotations: $\sim 70^\circ$ in the horizontal plane and $\sim 10^\circ$ in the vertical plane (7) (Figure 4B). These movements

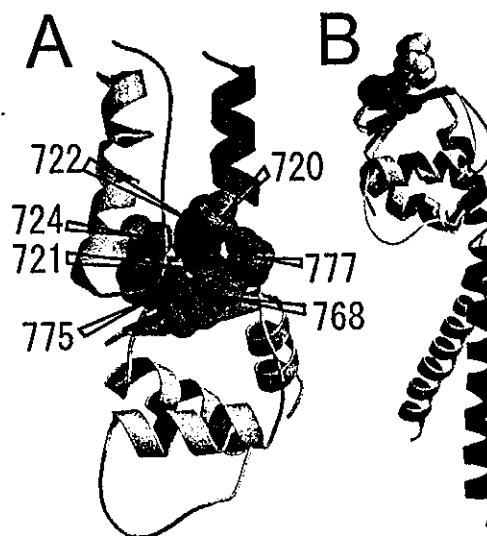


FIGURE 5: Structure and function of the small machine in the converter. (A) Enlarged view of the machine. The relay helix and loop are shown as a helical ribbon and a strand, respectively (both yellow). The SH1 helix is shown as a helical green ribbon. The three-stranded β -sheet is shown as plane ribbons (cyan), and all other structures in the converter are shown in white. Gly-720, Phe-721, Pro-722, Arg-724, Arg-768, Phe-775, and Arg-777 are presented as a CPK rendition. (B) Superposition of the converters in nucleotide-free and nucleotide-ligated myosin heads. In the former, the backbone atoms of the converter and a part of the lever arm are shown as blue and purple ribbons, respectively, and Gly-720 (orange), Phe-721 (red), and Phe-775 (pink) are presented as a CPK rendition. The latter is presented in the same manner, but all in white.

are enabled by the presence of Gly-720 (in the conserved Gly-Phe-Pro motif) at the helix-converter interface, and by Gly-709 of the helix (7). According to Rayment's studies of where crystal structures of the myosin head complexed with various ATP analogues belong in the catalytic cycle of ATP hydrolysis, the rotation of the converter domain occurs during the transition from the prehydrolysis state to the metastable state ($ADP\cdot P_i$) after hydrolysis, or it occurs during the open-to-closed conformational change of the binding cleft (5, 6, 32, 33).

The structure of the transmission system within the converter domain can be described in more detail as follows (Figure 5A). Three converter strands (residues 723–725, 766–770, and 773–777) form a β -sheet structure, and Phe-721 is in a compact hydrophobic cluster with Arg-768, Phe-775, and Arg-777 on the β -sheet. In the F721A system, the alanine substitute has no hydrophobic interaction with the cluster. The SH1 helix and the anterior part of the motor domain therefore lose contact with the converter stump and lever arm, which accounts for the uniform failure of this system in all of our tests of the lever arm swing and actin filament movements. In the F775A system, the normal hydrophobic interaction is absent, but Arg-724 and Arg-768 continue to form salt bridges with the relay helix; this might explain how the mutant continues to swing the lever arm and, albeit weakly, to move actin filaments. In normal operation, the side chain of Phe-775 is perpendicular to that of Phe-721, and makes direct contact with the distal end of the relay helix and the adjacent loop containing the ATP-sensitive Trp-512. These considerations suggest that, during the power stroke, the relay helix pushes the side chain of

Phe-775 with its tip, and rotates it around the principal axis of the SH1 helix.

We have further explored this speculation by comparing the structure of the relevant region (Gly-Phe-Pro motif and Phe-775) in its nucleotide-free and nucleotide-ligated states. The comparison reveals a largely unchanged structure, with the exception of a limited region in which a very small machine that accomplishes transmission seems to operate. The superimposition of images, as seen from the converter, reveals a rotation of $\sim 70^\circ$ around the principal axis of the SH1 helix in this area (Figure 4C and Movie S1 of the Supporting Information). Some movements are also observed near the relay helix and the SH1 helix. The rotation of this small machine is produced by the coordinated twisting motions of the two helices (circled arrows at the bottom), and further by the bending of the relay helix (translucent arrow). These motions of the transmission system can be created by the large Ramachandran angle changes at Gly-518 of the relay loop and at Gly-709 of the SH1 helix (7). The comparison between two converter structures in the nucleotide-free and nucleotide-ligated states revealed a high degree of similarity between states (Figure 5B), suggesting that the motion of the whole converter domain can largely be expressed as that of the little machine consisting of the Gly-Phe-Pro motif and Phe-775. Therefore, we suggest that this little machine is particularly important in positioning the converter-lever arm system. Other parts of the motor domain (for instance, the seven-stranded β -sheet structure core and the 25 kDa N-terminal domain) are also involved in the transmission of the force from the active site to the converter, but they seem to function as independent components of the overall motion.

Improved understanding of how the converter works gives a perspective of how overall transmission across myosin occurs. Closure of the cleft, which is induced by binding of the nucleotide to the active site, shifts the proximal end of the relay helix toward the active site (opaque arrow in Figure 4C), causing a clockwise rotation (as seen from the converter) (5, 34). These movements cause a large rotation of the little machine consisting of two Phe residues linked to a Gly, through the cooperation of the relay helix, the relay loop, and the SH1 helix. Finally, this rotation is transmitted to the rigidly attached lever arm by the converter. *In situ*, the relay helix transmits mechanical changes in both the actin-detached and actin-attached states (during the reverse and power strokes, respectively) (13, 21). However, under the circumstances that we describe, force is generated more effectively during the power stroke than during the reverse stroke. This is because the former occurs through a pushing motion of the side chain of Phe-775, whereas the latter occurs through a pulling motion, perhaps using hydrophobic interactions between the relay helix and the converter.

ACKNOWLEDGMENT

We thank K. Konishi for her early contribution to this study and T. Yanagida, H. Tanaka, and T. Watanabe for helping us assemble a microscope equipped with laser tweezers and a quadrant photodetector. We also thank T. J. Pearson for significant improvements to our manuscript.

SUPPORTING INFORMATION AVAILABLE

Movie showing a schematic three-dimensional model of the actions of the transmission machinery of myosin. This material is available free of charge via the Internet at <http://pubs.acs.org>.

REFERENCES

- Huxley, H. E. (1969) The mechanism of muscular contraction, *Science* **164**, 1356–1365.
- Huxley, A. F., and Simmons, R. M. (1971) Proposed mechanism of force generation in striated muscle, *Nature* **233**, 533–538.
- Rayment, I., Rypniewski, W. R., Schmidt-Bäse, K., Smith, R., Tomchick, D. R., Benning, M. M., Winkelmann, D. A., Wesenberg, G., and Holden, H. M. (1993) Three-dimensional structure of myosin subfragment-1: a molecular motor, *Science* **261**, 50–58.
- Rayment, I., Holden, H. M., Whittaker, M., Yohn, C. B., Lorenz, M., Holmes, K. C., and Milligan, R. A. (1993) Structure of the actin-myosin complex and its implications for muscle contraction, *Science* **261**, 58–65.
- Fisher, A. J., Smith, C. A., Thoden, J. B., Smith, R., Sutoh, K., Holden, H. M., and Rayment, I. (1995) X-ray structures of the myosin motor domain of *Dictyostelium discoideum* complexed with MgADP·BeF₃ and MgADP·AlF₄⁻, *Biochemistry* **34**, 8960–8972.
- Smith, C. A., and Rayment, I. (1996) X-ray structure of the magnesium(II)-ADP·vanadate complex of the *Dictyostelium discoideum* myosin motor domain to 1.9 Å resolution, *Biochemistry* **35**, 5404–5417.
- Dominguez, R., Freyzon, Y., Trybus, K. M., and Cohen, C. (1998) Crystal structure of a vertebrate smooth muscle myosin motor domain and its complex with the essential light chain: visualization of the pre-power stroke state, *Cell* **94**, 559–571.
- Houdusse, A., Szent-Györgyi, A. G., and Cohen, C. (2000) Three conformational states of scallop myosin S1, *Proc. Natl. Acad. Sci. U.S.A.* **97**, 11238–11243.
- Holmes, K. C., Angert, I., Kull, F. J., Jahn, W., and Schröder, R. R. (2003) Electron cryo-microscopy shows how strong binding of myosin to actin releases nucleotide, *Nature* **425**, 423–427.
- Bagshaw, C. R., and Trentham, D. R. (1974) The characterization of myosin-product complexes and of product-release steps during the magnesium ion-dependent adenosine triphosphatase reaction, *Biochem. J.* **141**, 331–349.
- Bagshaw, C. R., Eccleston, J. F., Eckstein, F., Goody, R. S., Gutfreund, H., and Trentham, D. R. (1974) The magnesium ion-dependent adenosine triphosphatase of myosin. Two-step processes of adenosine triphosphate association and adenosine diphosphate dissociation, *Biochem. J.* **141**, 351–364.
- Onishi, H., Ohki, T., Mochizuki, N., and Morales, M. F. (2002) Early stages of energy transduction by myosin: roles of Arg in switch I, of Glu in switch II, and of the salt-bridge between them, *Proc. Natl. Acad. Sci. U.S.A.* **99**, 15339–15344.
- Onishi, H., Mochizuki, N., and Morales, M. F. (2004) On the myosin catalysis of ATP hydrolysis, *Biochemistry* **43**, 3757–3763.
- Malnasi-Csizmadia, A., Woolley, R. J., and Bagshaw, C. R. (2000) Resolution of conformational states of *Dictyostelium* myosin II motor domain using tryptophan (W501) mutants: implications for the open-closed transition identified by crystallography, *Biochemistry* **39**, 16135–16146.
- Malnasi-Csizmadia, A., Kovacs, M., Woolley, R. J., Botchway, S. W., and Bagshaw, C. R. (2001) The dynamics of the relay loop tryptophan residue in the *Dictyostelium* myosin motor domain and the origin of spectroscopic signals, *J. Biol. Chem.* **276**, 19483–19490.
- Yanagisawa, M., Hamada, Y., Katsuragawa, Y., Imamura, M., Mikawa, T., and Masaki, T. (1987) Complete primary structure of vertebrate smooth muscle myosin heavy chain deduced from its complementary DNA sequence. Implications on topography and function of myosin, *J. Mol. Biol.* **198**, 143–157.
- Kojima, S., Fujiwara, K., and Onishi, H. (1999) SH1 (cysteine 717) of smooth muscle myosin: its role in motor function, *Biochemistry* **38**, 11670–11676.
- Kunkel, T. A., Roberts, J. D., and Zakour, R. A. (1987) Rapid and efficient site-specific mutagenesis without phenotypic selection, *Methods Enzymol.* **154**, 367–382.

19. Konishi, K., Kojima, S., Katoh, T., Yazawa, M., Kato, K., Fujiwara, K., and Onishi, H. (2001) Two new modes of smooth muscle myosin regulation by the interaction between the two regulatory light chains, and by the S2 domain, *J. Biochem.* **129**, 365–372.
20. Onishi, H., Maéda, K., Maéda, Y., Inoue, A., and Fujiwara, K. (1995) Functional chicken gizzard heavy meromyosin expression in and purification from baculovirus-infected insect cells, *Proc. Natl. Acad. Sci. U.S.A.* **92**, 704–708.
21. Suzuki, Y., Yasunaga, T., Ohkura, R., Wakabayashi, T., and Sutoh, K. (1998) Swing of the lever arm of a myosin motor at the isomerization and phosphate-release steps, *Nature* **396**, 380–383.
22. Stryer, L. (1978) Fluorescence energy transfer as a spectroscopic ruler, *Annu. Rev. Biochem.* **47**, 819–846.
23. Finer, J. T., Simmons, R. M., and Spudich, J. A. (1994) Single myosin molecule mechanics: piconewton forces and nanometre steps, *Nature* **368**, 113–119.
24. Molloy, J. E., Burns, J. E., Kendrick-Jones, J., Tregear, R. T., and White, D. C. (1995) Movement and force produced by a single myosin head, *Nature* **378**, 209–212.
25. Hiratsuka, T. (1983) New ribose-modified fluorescent analogs of adenine and guanine nucleotides available as substrates for various enzymes, *Biochim. Biophys. Acta* **742**, 496–508.
26. Batra, R., and Manstein, D. J. (1999) Functional characterization of *Dictyostelium* myosin II with conserved tryptophanyl residue 501 mutated to tyrosine, *Biol. Chem.* **380**, 1017–1023.
27. Onishi, H., Konishi, K., Fujiwara, K., Hayakawa, K., Tanokura, M., Martinez, H. M., and Morales, M. F. (2000) On the tryptophan residue of smooth muscle myosin that responds to binding of nucleotide, *Proc. Natl. Acad. Sci. U.S.A.* **97**, 11203–11208.
28. Marston, S. B., and Taylor, E. W. (1980) Comparison of the myosin and actomyosin ATPase mechanisms of the four types of vertebrate muscles, *J. Mol. Biol.* **139**, 573–600.
29. Majoul, I., Straub, M., Duden, R., Hell, S. W., and Soling, H. D. (2002) Fluorescence resonance energy transfer analysis of protein–protein interactions in single living cells by multifocal multiphoton microscopy, *J. Biotechnol.* **82**, 267–277.
30. Harada, Y., Noguchi, A., Kishino, A., and Yanagida, T. (1987) Sliding movement of single actin filaments on one-headed myosin filaments, *Nature* **326**, 805–808.
31. Kron, S. J., and Spudich, J. A. (1986) Fluorescent actin filaments move on myosin fixed to a glass surface, *Proc. Natl. Acad. Sci. U.S.A.* **83**, 6272–6276.
32. Gulick, A. M., Bauer, C. B., Thoden, J. B., and Rayment, I. (1997) X-ray structures of the MgADP, MgATP γ S, and MgAMPPNP complexes of the *Dictyostelium discoideum* myosin motor domain, *Biochemistry* **36**, 11619–11628.
33. Bauer, C. B., Holden, H. M., Thoden, J. B., Smith, R., and Rayment, I. (2000) X-ray structures of the apo and MgATP-bound states of *Dictyostelium discoideum* myosin motor domain, *J. Biol. Chem.* **275**, 38494–38499.
34. Fisher, A. J., Smith, C. A., Thoden, J., Smith, R., Sutoh, K., Holden, H. M., and Rayment, I. (1995) Structural studies of myosin:nucleotide complexes: a revised model for the molecular basis of muscle contraction, *Biophys. J.* **68**, 19S–26S.

BI048954F

A Novel Dynamin-associating Molecule, Formin-binding Protein 17, Induces Tubular Membrane Invaginations and Participates in Endocytosis*[§]

Received for publication, May 3, 2004, and in revised form, June 17, 2004
Published, JBC Papers in Press, July 12, 2004, DOI 10.1074/jbc.M404899200

Yuji Kamioka[‡], Shigetomo Fukuhara[‡], Hirofumi Sawa[§], Kazuo Nagashima[§], Michitaka Masuda[‡], Michiyuki Matsuda[¶], and Naoki Mochizuki[¶]

From the [‡]Department of Structural Analysis, National Cardiovascular Center Research Institute, 5-7-1 Fujishirodai, Suita, Osaka 565-8565, Japan, the [§]Laboratory of Molecular and Cellular Pathology, Hokkaido University School of Medicine, Sapporo 060-8638, Japan, and the [¶]Department of Tumor Virology, Research Institute for Microbial Disease, Osaka University, Osaka 565-0871, Japan

Dynamin associates with a variety of SH3 domain-containing molecules via a C-terminal proline-rich motif and takes part, with them, in endocytic processes. Here, we have investigated a new dynamin-associating molecule, formin-binding protein 17 (FBP17), involved in deforming the plasma membrane and in endocytosis. FBP17 formed tubular invaginations originating from the plasma membrane. Its N-terminal Fer/CIP4 homology domain, a coiled-coil domain, and a proline-rich motif were required for tubular invagination and self-assembly, by which tubular invagination might be induced. Using anti-FBP17 antibody, we detected positive immunoreactions in the testis that were restricted to the germ cells. We also detected FBP17 in the brain by immunoblotting and *in situ* hybridization. When COS cells expressing enhanced green fluorescent protein-tagged FBP17 were incubated with fluorescently labeled transferrin, epidermal growth factor, and cholera toxin, these molecules co-localized with FBP17-induced tubular invaginations, suggesting that FBP17 is involved in dynamin-mediated endocytosis in both a clathrin-dependent and -independent manner. These observations therefore indicate that FBP17 interacts with dynamin and regulates endocytosis by forming vesicotubular structures.

The plasma membrane changes its structure dynamically in response to a wide variety of extracellular stimuli that alter cell shape. Membrane extension, including the formation of filopodia and lamellipodia, is controlled by the Rho family GTPases Cdc42 and Rac, respectively (1). Rac and Cdc42 are involved in forming membrane protrusions essential for phagocytosis and macropinocytosis (2), whereas another GTPase, dynamin, has been implicated in producing membrane invaginations and vesicles from the plasma membrane (3).

* This work was supported in part by grants from the Ministry of Health, Labor, and Welfare of Japan; the Promotion of Fundamental Studies in Health Science of the Organization for Pharmaceutical Safety and Research of Japan; the Ministry of Education, Science, Sports, and Culture of Japan; the Cell Science Research Foundation; the Uehara Memorial Foundation; and the Takeda Medical Research Foundation. The costs of publication of this article were defrayed in part by the payment of page charges. This article must therefore be hereby marked "advertisement" in accordance with 18 U.S.C. Section 1734 solely to indicate this fact.

[§] The on-line version of this article (available at <http://www.jbc.org>) contains Supplemental Figs. 1 and 2 and Videos 1 and 2.

[¶] To whom correspondence should be addressed. Tel.: 81-6-6833-5012 (ext. 2508); Fax: 81-6-6835-5461; E-mail: nmochizu@ri.ncvc.go.jp.

Dynamin is a multidomain GTPase; it consists of a GTPase domain followed by a central domain lacking homology to any other proteins, a pleckstrin homology domain, an effector domain, and a C-terminal proline-rich motif (4). Dynamin-1 (neuron-specific), dynamin-2 (ubiquitously expressed), and dynamin-3 (expressed only in the testis, brain, and lung), constitute the dynamin family (5–7). These proteins are essential for clathrin-dependent and also caveolae-mediated endocytosis (reviewed in Refs. 8 and 9). In addition, association of dynamin with Src homology 3 (SH3)¹ domain-containing molecules has been shown to modulate endocytosis since the C-terminal proline-rich motif provides an SH3 domain-binding site (10). The dynamin-binding molecules amphiphysin, endophilin, intersectin, and PACSIN/syndapin have been reported to be involved in modulating dynamin-dependent endocytosis (4, 11).

Formin-binding protein 17 (FBP17) consists of an N-terminal Fer/Cdc42-interacting protein 4 (CIP4) homology (FCH) domain followed by the first coiled-coil domain, a proline-rich motif, the second coiled-coil domain, a Rho family protein-binding domain (RBD), and a C-terminal SH3 domain. FBP17 was originally isolated as a molecule that binds to the proline-rich region of formin (12). FBP17 is fused to mixed-lineage leukemia in acute myeloid leukemia (13). However, its function remains unclear.

Based on domain structure, it is evident that FBP17 is closely related to CIP4. CIP4 localizes to microtubules presumably via its N-terminal FCH domain, binds to Cdc42 via the central region corresponding to the RBD of FBP17, and associates with Wiskott-Aldrich syndrome protein via a C-terminal SH3 domain (14). A CIP4 homolog, Rapostlin, consists of an N-terminal FCH domain, an RBD, and a C-terminal SH3 domain similar to CIP4. Rapostlin has been identified as an effector that binds to the Rho family GTPase Rnd2 (15). Rapostlin shares 93% amino acid identity with FBP17, indicating that FBP17 is likely to be an ortholog of Rapostlin. Like CIP4, Rapostlin partially localizes to microtubules via its N-terminal FCH domain (15). Although the FCH domain is thought to be a microtubule-targeting domain (16), we have previously shown

¹ The abbreviations used are: SH3, Src homology 3; FBP17, formin-binding protein 17; CIP4, Cdc42-interacting protein 4; FCH, Fer/CIP4 homology; RBD, Rho family protein-binding domain; EGF, epidermal growth factor; CTB, cholera toxin subunit B; EGFP, enhanced green fluorescent protein; DiIC₁₆(3), 1,1'-dihexadecyl-3,3',3'-tetramethylindocarbocyanine perchlorate; GFP, green fluorescent protein; DMEM, Dulbecco's modified Eagle's medium; PBS, phosphate-buffered saline; GST, glutathione S-transferase; M-amphiphysin-2, muscle amphiphysin-2.

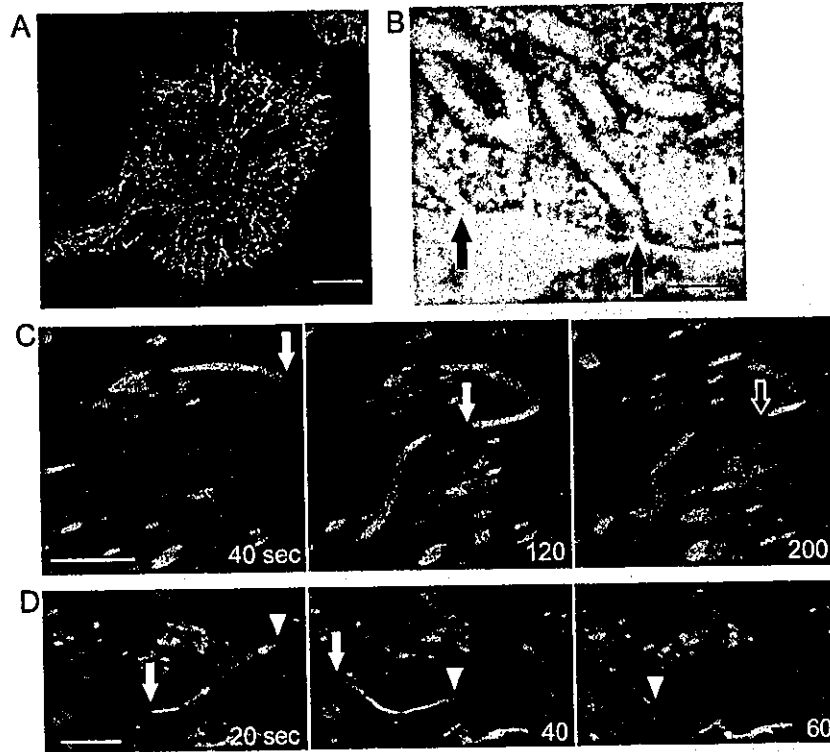


FIG. 1. FBP17 generates tubules growing from the plasma membrane to inside of the cells. **A**, COS-1 cells cultured on collagen-coated glass-bottom dishes were transfected with an EGFP-tagged FBP17-expressing plasmid. Cells were imaged on an Olympus IX-71 epifluorescence microscope. *Bar* = 10 μ m. **B**, COS-1 cells expressing EGFP-tagged FBP17 was examined with a Hitachi H-800 electron microscope. Tubular structures originating from the plasma membrane were observed as indicated by the arrows. *Bar* = 1 μ m. **C**, COS-1 cells expressing EGFP-tagged FBP17 were monitored by time-lapse imaging every 20 s. *Closed arrows* indicate the growth of cylindrical structure toward the inside of the cell. The *open arrow* denotes the retracting tubule in the cell. The time that elapsed from the beginning of the observation is shown at the right bottom of each panel. *Bar* = 5 μ m. A series of these images has been converted to a video file (Supplemental Video 1). **D**, other COS-1 cells expressing EGFP-tagged FBP17 were monitored by time-lapse imaging. *Closed arrowheads* and *arrows* indicate the origin and the end of the tubule, respectively. Note that the tubule was internalized. A series of these images has been converted to a video file (Supplemental Video 2). *Bar* = 5 μ m.

that the FCH domain of Fer tyrosine kinase is not required for localization of Fer to microtubules (17). In addition, the dynamin-associating molecule PACSIN/syndapin, which contains an N-terminal FCH domain, does not localize to microtubules (18). Since both FBP17 and PACSIN contain an N-terminal FCH domain, a coiled-coil domain, and a C-terminal SH3 domain, it seems probable that FBP17 is also involved in dynamin-regulated endocytosis.

In this study, we demonstrate that FBP17 induces the plasma membrane to form tubular structures and that FBP17 associates with a C-terminal proline-rich motif of dynamin. Transferrin, epidermal growth factor (EGF), and cholera toxin subunit B (CTB) are taken up along with FBP17-induced tubules in COS-1 cells expressing FBP17, suggesting that FBP17 is involved in dynamin-mediated endocytosis.

EXPERIMENTAL PROCEDURES

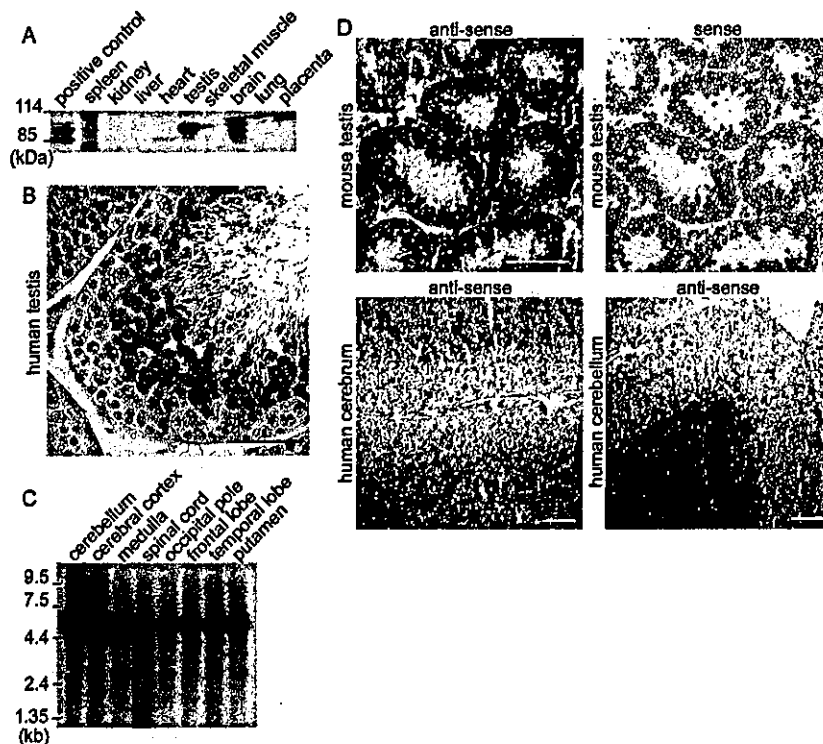
Plasmids—Full-length *FBP17* and *PACSIN-1* cDNAs were amplified by PCR from a human brain cDNA library (Clontech). PCR-amplified DNAs encoding FBP17 and its truncated mutants FBP17-N1 (amino acids 1–250), FBP17-N2 (amino acids 1–377), FBP17-C1 (amino acids 291–616), FBP17-dFCH (amino acids 80–616) were inserted into pCA-EGFP, a protein expression vector tagged at its N terminus with enhanced green fluorescent protein (EGFP) and derived from vector pCAGGS (19). A DNA fragment encoding a modified form of FBP17 referred to as FBP17-P597L, in which Leu is substituted for Pro⁵⁹⁷ in the SH3 domain, was amplified by PCR-based mutagenesis and ligated into pCA-EGFP. Full-length *PACSIN-1* cDNA was likewise inserted into pCA-EGFP. pCXN2-FLAG-FBP17-N2 is derived from pCAGGS and expresses N-terminally FLAG-tagged FBP17-N2. A cDNA encoding the SH3 motif of FBP17 (amino acids 534–616) and a cDNA encoding a nonfunctional SH3 domain (P597L) of FBP17 were amplified by PCR and ligated into pGEX-4T3 (Amersham Biosciences, Little Chalfont, Buckinghamshire, United Kingdom). Full-length *dynamin-1* and *dy-*

namin-2 cDNAs were obtained by PCR from a human heart cDNA library and ligated into pCA-EGFP and pCXN2-FLAG. Full-length *dynamin-3* cDNA was amplified by PCR using KIAA0820 (a kind gift from Kazusa DNA Research Institute, Chiba, Japan) as a template and ligated into pEGFP-C1 (Clontech). cDNA encoding a GTPase-deficient mutant of dynamin-1 with Ala substituted for Lys⁴⁴ (K44A) was amplified by PCR-based mutagenesis and ligated into pERed-NLS. pERed-NLS-dynamin-1-K44A expresses both FLAG-tagged dynamin-1-K44A and internal ribosomal entry signal-driven DsRed-Express fused with a nuclear localization signal (Clontech). pBluescript (Stratagene, La Jolla, CA) containing nucleotides 809–1851 of FBP17 was used to produce both antisense and sense riboprobes for *in situ* hybridization. All of the DNA fragments amplified by PCR were ligated into the pCR4blunt-TOPO vector (Invitrogen) and confirmed by sequencing with an Applied Biosystems ABI Prism 3700 sequencer.

Reagents and Antibodies—DiI₁₆(3), Alexa 546-conjugated transferrin, Texas Red-conjugated EGF, Alexa 555-conjugated CTB, Alexa 546-conjugated goat anti-mouse IgG, and Alexa 488-conjugated goat anti-rabbit IgG were purchased from Molecular Probes, Inc. (Eugene, OR). Anti- β -tubulin antibody, anti-vimentin antibody, rhodamine-conjugated phalloidin, and anti-FLAG antibody M2 were from Sigma. Anti-KDEL antibody was from Stressgen Biotech Corp. Anti-dynamin-2 antibody was from Santa Cruz Biotechnology (Santa Cruz, CA). Protein A-Sepharose, protein G-Sepharose, and glutathione-Sepharose were from Amersham Biosciences. The digoxigenin-labeled riboprobe synthesis kit and the random-primed DNA labeling kit were from Roche Diagnostics (Basel, Switzerland). [α -³²P]dCTP (EasyTidesTM) was from PerkinElmer Life Sciences. Anti-green fluorescent protein (GFP) antibody was developed in our laboratory, and anti-FBP17 antibody was produced by immunizing rabbits with a keyhole limpet hemocyanin-coupled synthetic peptide (CAQDRESPDGSYTTEEQSQES) corresponding to amino acids 506–525 of FBP17.

Cell Culture and Transfection—293T cells (a gift from B. J. Meyer, University of Connecticut, Storrs, CT) and COS-1 cells (American Type Culture Collection, Manassas, VA) were maintained in Dulbecco's modified Eagle's medium (DMEM) supplemented with 10% fetal

FIG. 2. FBP17 is expressed in the testis and brain. *A*, proteins from the mouse tissues indicated were subjected to SDS-PAGE followed by immunoblotting with anti-FBP17 antibody. A lysate of 293T cells expressing FLAG-tagged FBP17 was used as positive control. Molecular mass markers are on the left. *B*, the sections of human testis fixed with Bouin's solution were immunostained with anti-FBP17 antibody and visualized with diaminobenzidine (brown). Staining can be seen in all cells except those in the innermost and outermost layers. *Bar* = 50 μ m. *C*, an RNA blot (human multiple-tissue blot) was probed with radiolabeled FBP17 cDNA. 6.0-kb transcription products were detected in all lanes with RNAs prepared from the various regions of the brain as indicated. The detection procedure is described under "Experimental Procedures." *D*, frozen sections from the tissues indicated were probed with digoxigenin-labeled FBP17 antisense or sense probes. FBP17 mRNA that hybridized with the probe appears dark purple. *Bars* = 200 μ m.



bovine serum. Cells were transfected using LipofectAMINE 2000 (Invitrogen).

Cell Membrane Staining—COS-1 cells cultured on glass-bottom dishes were washed three times with DMEM without phenol red, incubated with DMEM containing 10 μ g/ml DiIC₁₆(3) for 10 min, rinsed twice with phosphate-buffered saline (PBS), fixed with 2% formaldehyde in PBS, and examined by confocal fluorescence imaging.

Transferrin, EGF, and CTB Uptake—COS-1 cells expressing EGFP-FBP17 were serum-starved in DMEM for 1 h and incubated with 25 μ g/ml Alexa 546-conjugated transferrin for 20 min at either 37 °C or 4 °C and with 1 ng/ml Texas Red-conjugated EGF or 1 μ g/ml Alexa 555-conjugated CTB at 37 °C. After rinsing three times with PBS and reducing surface labeling using 50 mM deferoxamine mesylate-containing buffer (150 mM NaCl, 2 mM CaCl₂, and 25 mM sodium acetate/acetic acid, pH 4.5), the cells were fixed with 2% formaldehyde in PBS and subjected to fluorescence imaging. Images of fluorescence-conjugated transferrin, EGF, or CTB were obtained with an Olympus IX-71 epifluorescence microscope equipped with a cooled charge-coupled camera (CoolSNAP-HQ, Roper Scientific, Trenton, NJ).

Immunoblotting and Immunoprecipitation—Immunoblotting and immunoprecipitation were performed as described previously (17). Briefly, 293T cells were washed with PBS and lysed with buffer containing 150 mM NaCl, 20 mM Tris-HCl (pH 7.5), 1.5 mM MgCl₂, 1% Triton X-100, and protease inhibitor mixture (Roche Diagnostics). Pre-cleared cell lysates were immunoprecipitated with antibodies as indicated together with protein A- or G-Sepharose. Precipitates were subjected to SDS-PAGE followed by immunoblotting with antibodies as indicated. Proteins that reacted with the primary antibody recognized by the peroxidase-conjugated secondary antibody and that were species-matched were visualized with the ECL system (Amersham Biosciences) and a LAS-1000 image analyzer (Fuji Film, Tokyo, Japan). Tissues from BALB/c mice were rinsed with PBS and homogenized in lysis buffer (62.5 mM Tris-HCl (pH 6.8), 10% glycerol, 2% SDS, and bromophenol). The homogenates were centrifuged at 100,000 \times g for 10 min. The pellets were fractionated by SDS-PAGE and immunoblotted with anti-FBP17 antibody.

Immunohistochemistry and Electron Microscopy—Human testis fixed with Bouin's solution and embedded in paraffin was sectioned, deparaffinized, and immunostained with anti-FBP17 antibody. Immunoreactivity detected by the peroxidase-conjugated secondary antibody was visualized with 1 mg/ml diaminobenzidine. Sections were counterstained with hematoxylin. For electron microscopy, COS-1 cells expressing EGFP-FBP17 were fixed with 2.5% glutaraldehyde and post-fixed in 1% OsO₄ followed by embedding in epoxy resin. Ultrathin sections on nickel grids were immersed in target retrieval solution (DakoCytomation, Kyoto, Japan). After washing with distilled water

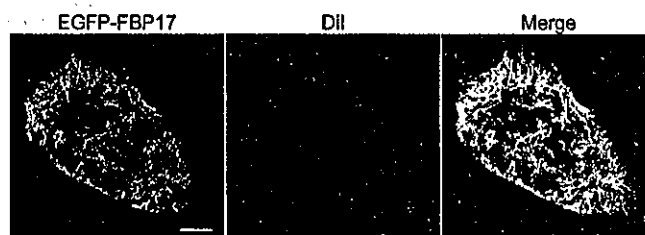


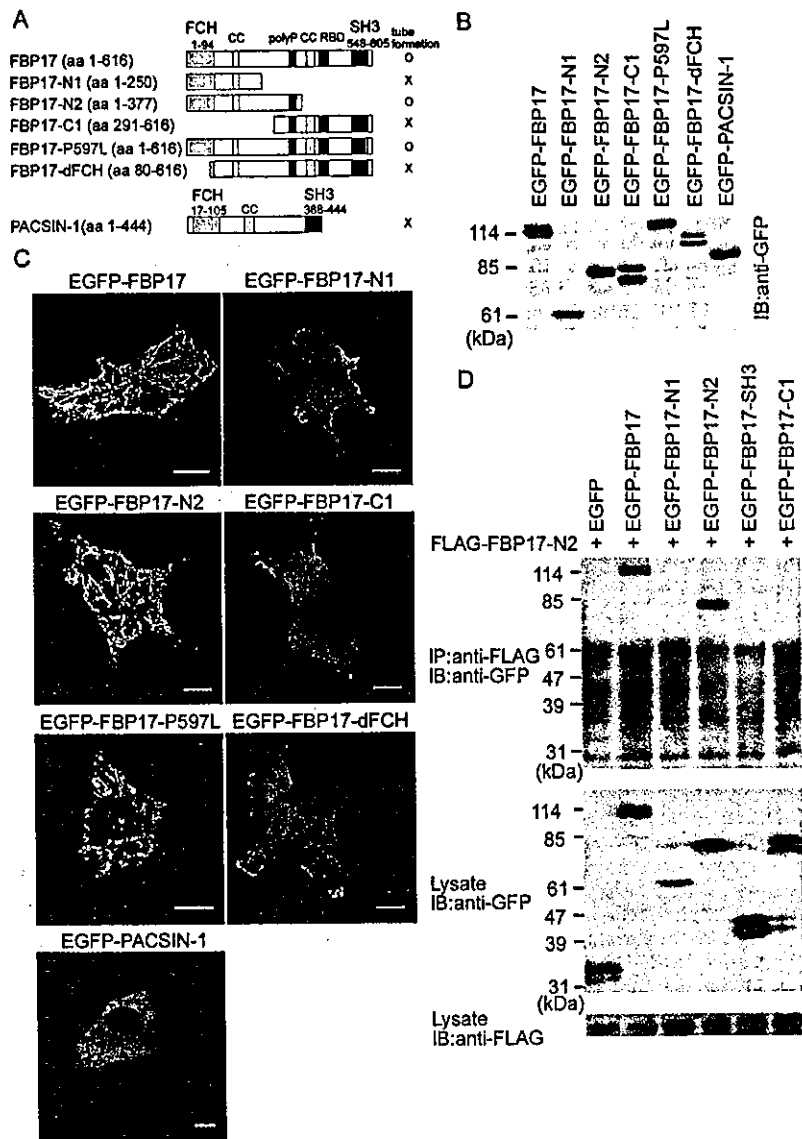
FIG. 3. FBP17-induced tubular structures are plasma membrane invaginations. COS-1 cells expressing EGFP-tagged FBP17 were incubated with DiIC₁₆(3) for 10 min and fixed with PBS containing 2% formaldehyde. GFP images (EGFP-FBP17) and DiIC₁₆(3)-stained images (DiI) were obtained using an Olympus BX50EI confocal microscope and superimposed (Merge). *Bar* = 10 μ m.

and drying, sections were stained with both uranyl acetate and lead citrate and examined with a Hitachi H-800 electron microscope.

Northern Blot Analysis and In Situ Hybridization—A multiple-tissue Northern blot membrane (Human Brain II, Clontech) was prehybridized, followed by high stringency hybridization with an [α -³²P]dCTP-labeled FBP17 probe and washing with buffer containing appropriate concentrations of SSC and SDS. RNA hybridized with the radiolabeled probe was detected with a BAS-5000 imaging system (Fuji Film). *In situ* hybridization was performed as described previously (20). Briefly, mouse testis and human brain were embedded in Tissue-Tec OCT compound and frozen in liquid nitrogen. Cryostat sections were fixed in 4% paraformaldehyde, prehybridized, and hybridized overnight at 72 °C with digoxigenin-labeled riboprobe in hybridization buffer (50% formamide, 5 \times SSC, 5 \times Denhardt's solution, and 500 μ g/ml tRNA). The sections were washed with 0.2 \times SSC and incubated with anti-digoxigenin antibody. The signal was visualized with nitro blue tetrazolium chloride/5-bromo-4-chloro-3-indolyl phosphate solution containing 0.24 mg/ml levamisole.

Confocal Microscopy and Fluorescence Imaging—Cells cultured on glass-bottom dishes and transfected with pCA-EGFP-FBP17 for 24 h were fixed with 2% formaldehyde and permeabilized with 0.1% Triton X-100. For anti-vimentin antibody immunostaining, cells were fixed with methanol. The permeabilized cells were incubated with anti- β -tubulin, anti-KDEL, or anti-vimentin antibody followed by Alexa 546-conjugated goat anti-mouse IgG to visualize tubulin, the endoplasmic reticulum, and vimentin. Actin was visualized with rhodamine-conjugated phalloidin. Fluorescent images of EGFP and of Alexa 546 or rhodamine were obtained with an Olympus BX50EI confocal microscope controlled by Fluoview (Olympus, Tokyo) as described previously

FIG. 4. The N terminus of FBP17 is essential for FBP17-induced tubule formation. A, shown is a schematic illustration of the structure of FBP17 consisting of an N-terminal FCH domain followed by a proline-rich motif (polyproline (*polyP*)) flanked by coiled-coil domains (CC), an RBD, and a C-terminal SH3 domain. Amino acid (aa) numbers are given on the left and at the top. Structurally related PACSIN-1 is indicated at the bottom. The results in C are summarized on the right. B, 293T cells were transfected with a plasmid expressing N-terminally EGFP-tagged proteins as indicated. Lysates of the transfectants were subjected to SDS-PAGE followed by immunoblotting with anti-GFP antibody. C, COS-1 cells transfected with the plasmids indicated were imaged by confocal microscopy (Olympus BX50EI). Note that essential domains required for tube formation are the FCH domain, the first coiled-coil domain, and the polyproline motif. Bars = 10 μ m. D, 293T cells were transfected with the plasmids indicated. Cell lysates were subjected either to immunoprecipitation (IP) followed by immunoblotting (IB) or directly to immunoblotting using the antibodies indicated. Note that the FCH domain, the first coiled-coil domain, and the polyproline motif are sufficient for dimerization of FBP17. The immunoblot results are representative of three independent experiments.



(21). Time-lapse fluorescence imaging was performed as described previously (21). Briefly, COS-1 cells expressing EGFP-FBP17 were cultured on a collagen-coated glass-bottom dish in DMEM/nutrient mixture F-12 (Invitrogen) supplemented with 10% fetal bovine serum, 2 mM L-glutamine, and 10 mM HEPES without phenol red. The cells were imaged using an Olympus IX-71 inverted microscope with a 75-watt xenon arc lamp equipped with a CoolSNAP-HQ cooled charge-coupled camera and two shutters, controlled by MetaMorph Version 5.0 software (Roper Scientific). To localize EGFP-tagged proteins, we obtained a fluorescent image every 20 s. Time-lapse images were converted to video format with MetaMorph Version 5.0 software.

Quantitative Analysis of the Effect of Dynamin-1-K44A on Internalization of FBP17-induced Tubules—To examine the effect of dynamin-1-K44A on FBP17-induced tubule formation, COS-1 cells were cotransfected with either pCA-EGFP-FBP17 or pCA-EGFP-FBP17-P597L and pERed-NLS-dynamin-1-K44A. Both EGFP images and DsRed images were obtained using an Olympus IX-71 epifluorescence microscope. EGFP intensity, which reflects the intracellular accumulation of all tubular invaginations that were not processed in the endocytic pathway, was calculated by measuring the total intensity of the cell divided by the total cell area using MetaMorph Version 5.0 software. Data obtained from 50 cells were averaged, and statistical significance was evaluated by Student's *t* test.

RESULTS

FBP17 Forms Tubular Invaginations in Living Cells—FBP17 has an N-terminal FCH domain. It has been suggested that this domain is a microtubule-targeting domain (16). Indeed, a previous study revealed that Rapostlin, a rat ortholog of

human FBP17, partially localizes to microtubules (15). We therefore examined the localization of EGFP-tagged FBP17 in COS-1 cells (Fig. 1A) and found that it was located in cylindrical fiber structures of the cytoplasm. It was not present in the cytoskeleton, including microtubules, actin stress fibers, and intermediate filaments, or in the endoplasmic reticulum of COS-1 cells (Supplemental Fig. 1). When FLAG-tagged FBP17 was expressed in the cells, similar cylindrical fiber-like immunostaining was observed in the cytoplasm (Supplemental Fig. 2B).

We examined whether the cylindrical fiber structures are tubes. COS-1 cells transfected with a plasmid expressing EGFP-FBP17 were examined with an electron microscope. The open ends and the blind ends of the tubular structures induced by FBP17 were in the plasma membrane and cytoplasm, respectively (Fig. 1B). To examine how cylindrical fiber-like structure developed in the living cells, we monitored EGFP-FBP17 in COS-1 cells by time-lapse fluorescence microscopy. The fibers arose from the cell periphery, grew toward the center of the cell, and sometimes contracted back toward the periphery (Fig. 1C and Supplemental Video 1). We further noticed that some EGFP-FBP17-marked tubules were internalized instead of being contracted (Fig. 1D and Supplemental Video 2). The GFP-expressing plasmid used as a negative control did not induce any tubule formation. These results indicate